Distributions of aluminum, manganese, cobalt, and lead in the western South Pacific: Interplay between the South and North Pacific

AUTHOR(S):

Zheng, Linjie; Minami, Tomoharu; Takano, Shotaro; Sohrin, Yoshiki

CITATION:

Zheng, Linjie ...[et al]. Distributions of aluminum, manganese, cobalt, and lead in the western South Pacific: Interplay between the South and North Pacific. Geochimica et Cosmochimica Acta 2022, 338: 105-120

ISSUE DATE:

2022-12-01

URL:

http://hdl.handle.net/2433/282033

Geochimica et Cosmochimica Acta 338 (2022) 105–120

Contents lists available at ScienceDirect

Geochimica et Cosmochimica Acta

journal homepage: www.elsevier.com/locate/gca

Distributions of aluminum, manganese, cobalt, and lead in the western South Pacific: Interplay between the South and North Pacific

Linjie Zheng [a], Tomoharu Minami [a,b], Shotaro Takano [a], Yoshiki Sohrin [a,*]

[a] Institute for Chemical Research, Kyoto University, Gokasho, Uji, Kyoto 611-0011, Japan
[b] Engineering and Technology Department, Kanazawa University, Kakuma, Kanazawa, Ishikawa 920-1192, Japan

ARTICLE INFO

Article history:
Received 21 January 2022
Accepted 12 October 2022
Available online 18 October 2022
Associate editor: Claudine Stirling

Keywords:
GEOTRACES
Scavenged elements
Biogeochemical cycling
Weathering
Anthropogenic pollution

ABSTRACT

Aluminum (Al), manganese (Mn), cobalt (Co), and lead (Pb) are strongly scavenged from seawater. We reported that each element is uniquely related to ocean circulation in the North Pacific (Zheng et al., 2019). Herein, we present the full-depth distributions of these elements in the western South Pacific, which include meridional sections along 170°W (GEOTRACES GP19). We determined dissolved (d) and total dissolvable (td) concentrations using filtered and unfiltered seawater without UV treatment, and we calculated labile particulate (lp) concentrations as the difference between td and d concentrations. This and the previous studies present the basin scale distributions, which enable us to investigate first order processes that drive the biogeochemistry of Al, Mn, Co, and Pb in the Pacific Ocean. The meridional section of dAl along 170°W (GP19)-160°W (GPc06) from 64°S to 54°N indicates that elevated concentrations (maximum 6.1 nmol/kg) occur between 40°S and 10°S from surface to bottom. However, the maxima of lpAl occur at high latitudes. The lpAl/tdAl ratio has a minimum of 0.26 ± 0.12 (ave ± sd, n = 116) in the zone from 30°S to 0°S. Based on these results, we propose a hypothesis that weathering on land has a significant effect on the distribution of Al in the ocean. Intensive weathering on tropical and subtropical islands and Australia forms kaolinite-dominated soils and laterite. This process provides dAl and kaolinite to the ocean. The supply of kaolinite results in kaolinite-dominated sediments that become a major bottom source for dAl. In contrast, strong sources of Mn and Co are continental shelves around the northern boundary. Dissolved Mn and dCo are released from sediments by manganese reduction and carried by intermediate water circulation. In particular, dCo spreads in the North Pacific Intermediate Water (NPIW), Equatorial Pacific Intermediate Water (EqPIW), and Antarctic Intermediate Water (AAIW); 23–59 pmol/kg at a potential density anomaly (σ_θ) of 27.0. This is partly owing to the uptake of dCo by phytoplankton and remineralization from settling particles. The dPb concentrations are 10 ± 6 pmol/kg (n = 397) in the South Pacific and 30 ± 20 pmol/kg (n = 566) in the North Pacific. The distribution of dPb is characterized by a maximum in the Subtropical Mode Water (SMW) and Central Mode Water (CMW) with σ_θ∼26 in the North Pacific. These results indicate that Pb is predominantly supplied by anthropogenic aerosols from Asia and Russia to the Pacific Ocean. Because Pb is not actively taken up by phytoplankton, Pb enters mode waters during winter convection and is transported with mode waters.

1. Introduction

Aluminum (Al), manganese (Mn), cobalt (Co), and lead (Pb) are generally classified as scavenged elements, of which dissolved (d) species are adsorbed on particles and removed from the ocean with a residence time of ∼ 10^2–10^3 years, resulting in high concentrations near sources (Bruland and Lohan, 2003; Chester, 2000). Aluminum is a tracer of lithogenic materials. Manganese is a tracer of the reduction reaction in the ocean, such as photochemical reduction in surface water, manganese reduction in sediments, and reduction during hydrothermal fluid formation. Manganese and Co are essential elements for organisms, and Pb is a tracer of anthropogenic pollution. Recently, we reported the distributions of d, total dissolvable (td), and labile particulate (lp) species of Al, Mn, Co, and Pb in the North Pacific Ocean (Zheng et al., 2019), demonstrating that each scavenged element is distributed uniquely and related to water masses and ocean circulation. The study herein is subsequent to the previous study and is conducted in the western South Pacific. The objective is to present the whole basin scale distribu-

* Corresponding author.
E-mail address: sohrin@scl.kyoto-u.ac.jp (Y. Sohrin).

https://doi.org/10.1016/j.gca.2022.10.022
0016-7037/

tions and to investigate first order processes that drive the biogeochemistry of Al, Mn, Co, and Pb in the Pacific Ocean.

Because we presented a historical review of the chemical oceanography of Al, Mn, Co, and Pb in the previous paper, we describe below recently reported and highly relevant studies. GEOTRACES is an international program that aims to improve the understanding of biogeochemical cycles and large-scale distribution of trace elements and their isotopes in the marine environment (https://www.geotraces.org). GEOTRACES released the third version of its intermediate data product (IDP2021), which contained three transects in the South Pacific. GP16 is a zonal transect along 10°S from Peru to 150°W, where the distributions of dAl (Ho et al., 2019), dMn (Resing et al., 2015), dCo (Hawco et al., 2016), dPb (Boyle et al., 2020; Hawco et al., 2016), and particulate metals (Lam et al., 2018) have been reported. GP13 is a zonal transect along 10°S from Australia to 170°W, of which dMn and dPb are included in the IDP2021. GP19 is a meridional section along 170°W, of which dAl, dMn, and dPb are included in the IDP2021 and discussed in this paper. Additional data included in the IDP2021 are as follows: dMn and dCo (Hawco et al., 2020) from GPc03 in the equatorial Pacific, dAl (Remenyi et al., 2012), dMn, and dPb from GIPY06 and GS01 to the south of Tasmania.

Basin scale meridional and zonal sections of dAl have been obtained from the Atlantic Ocean (Measures et al., 2015; Middag et al., 2015). The first global oceanic compilation of dAl data was recently reported (Menzel Barraqueta et al., 2020). Based on these observations, the following mechanisms have been proposed to control dAl cycling in the ocean: dust deposition as a surface source, association with biogenic silica as a scavenger, and resuspension as a bottom source (van Hulten et al., 2014). Data of dAl were used to estimate atmospheric dust deposition over the Atlantic Ocean (Menzel Barraqueta et al., 2019). Dissolved Al was linearly correlated with $Si(OH)_4$ in the North Atlantic, where deep water mass age is young (Middag et al., 2015). However, uncoupling between dAl and $Si(OH)_4$ was observed in the South Atlantic due to mixing of young and old water masses. The uncoupling was also observed in the Southern Ocean (Middag et al., 2011; Middag et al., 2012). The enrichment of dAl in the Arctic Ocean was observed, which cannot be explained by the water column remineralization of vertically transported biological material (Measures and Hatta, 2021; Middag et al., 2009). The suggested mechanisms for the enrichment of dAl were the input of terrigenous particles via deep convection (Middag et al., 2009) and the dissolution of amorphous aluminosilicates that are produced within the sedimentary pore water by reverse weathering (Measures and Hatta, 2021).

The first global ocean circulation model of Mn has been reported (van Hulten et al., 2017). This model included oxidation and (photo)reduction, aggregation and settling, as well as biological uptake by phytoplankton and remineralization. A linear relationship between dMn and apparent oxygen utilization (AOU) was found in deep waters in the tropical Pacific, which was attributed to remineralization of dMn (Chen and Wu, 2019). The co-limitation of phytoplankton growth by Mn was observed in the central Drake Passage (Browning et al., 2021).

It has been reported that UV irradiation prior to preconcentration is necessary for the analysis of total dCo (Biller and Bruland, 2012; Milne et al., 2010; Saito and Moffett, 2001). Irradiation of UV is required for the analysis of dCo in the Sampling and Sample-handling Protocols for the GEOTRACES Cruises (https://geotracesold.sedoo.fr/Cookbook.pdf). Using UV-dCo data, the scavenging rates of Co were estimated throughout the global ocean (Hawco et al., 2018). Many laboratories routinely use UV irradiation without any contamination. However, we refrained from using UV irradiation to minimize possible contamination and to avoid the unknown effects of UV irradiation on the multielemental determination of trace metals (Wuttig et al., 2019; Zheng et al., 2019). The data for dCo without UV treatment (non-UV-dCo) have been reported from the Antarctic Ocean (Butler et al., 2013), the Atlantic and Southern Ocean (Bown et al., 2011), the Indian Ocean (Vu and Sohrin, 2013), the North Pacific (Zheng et al., 2019), and the South Pacific herein. The data of non-UV-dCo are consistent with each other and can be useful for oceanographic studies. We think the data compilation of UV-dCo and non-UV-dCo will contribute to further understanding of dCo speciation.

2. Materials and methods

2.1. Study area and oceanographic setting

This study was conducted on the Japanese GEOTRACES cruises (KH-14–6) of R/V *Hakuho Maru* from 15 December 2014 to 6 February 2015. A number of maps and figures were prepared using the Ocean Data View software (Schlitzer, 2021). Fig. 1a shows the sampling stations and surface currents with the annually averaged surface $Si(OH)_4$ concentrations from the World Ocean Atlas V2 2013 (https://www.nodc.noaa.gov). The station GR04 was occupied in the Melanesian Basin, GR05 was in the North Fiji Basin, GR06 was in the South Fiji Basin, GR08 and GR09 were occupied above the Pacific-Antarctic Ridge, and the other stations were occupied in the Southwest Pacific Basin. We found the Subtropical Front (STF) between GR11 and GR10, the Subantarctic Front (SAF) between GR10 and GR07, and the Antarctic Polar Front (APF) between GR09 and GR08. Stations GR08–GR21 along 170°W form the GEOTRACES GP19 transect. To the south of GR18, sea surface currents flow eastward as a part of the Antarctic Circumpolar Current, the Subtropical Gyre, and the East Australian Current (EAC) System (Reid, 1986, 1997; Talley et al., 2011). The South Equatorial Current (SEC) flows westward around stations GR18–GR20. The Equatorial Under Current (EUC) flows eastward around GR21.

The Tonga-Kermadec Arc is an area of active volcanism. A submarine volcano Hunga Tonga-Hunga Ha'apai that is located 67 km north of Tonga's main island caused eruption on 15 January 2022, which was rated at least a VEI-5 (https://volcano.si.edu/volcano.cfm?vn=243040&vtab=Eruptions). A large amount of ash, pumice, and hyaloclastites deposited in this area (Yuen et al., 2022). The Lau Basin hosts a complicated pattern of volcanism, including arc, back-arc, and hotspot affinities (Lupton et al., 2015). The distribution of δ^3He shows that hydrothermal plumes from the Lau Basin spread in this region (Jenkins et al., 2019; Lupton et al., 2004) (Fig. 1b). The North Fiji Basin is a back-arc basin, near the center of which there is an active spreading ridge, and hydrothermal plumes were observed in this basin (Sedwick et al., 1990). In the Southwest Pacific Basin, there are anticyclonic geostrophic circulations flowing along the Tonga-Kermadec Arc at intermediate depths (Kawabe and Fujio, 2010; Reid, 1986) (Fig. 1b). Argo floats deployed west of the Arc go west (https://www.coriolis.eu.org/Data-Products/Data-Delivery/Data-selection; https://fleetmonitoring.euro-argo.eu/dashboard). Those deployed east of the Arc travel west, and when they reach the Arc they seem to then cycle back to the east into the open ocean. These data suggest that the anticyclonic circulation carries hydrothermal and terrigenous materials from west to the Southwest Pacific Basin.

The sectional distribution of salinity along the GP19 transect is shown in Fig. 1c. Water masses, such as the South Pacific Subtropical Mode Water (SPSTMW), Subantarctic Mode Water (SAMW), Antarctic Intermediate Water (AAIW), Equatorial Pacific Intermediate Water (EqPIW), Upper Circumpolar Deep Water (UCDW), Pacific Deep Water (PDW), and Lower Circumpolar Deep Water (LCDW) were identified on the transect. The major properties of

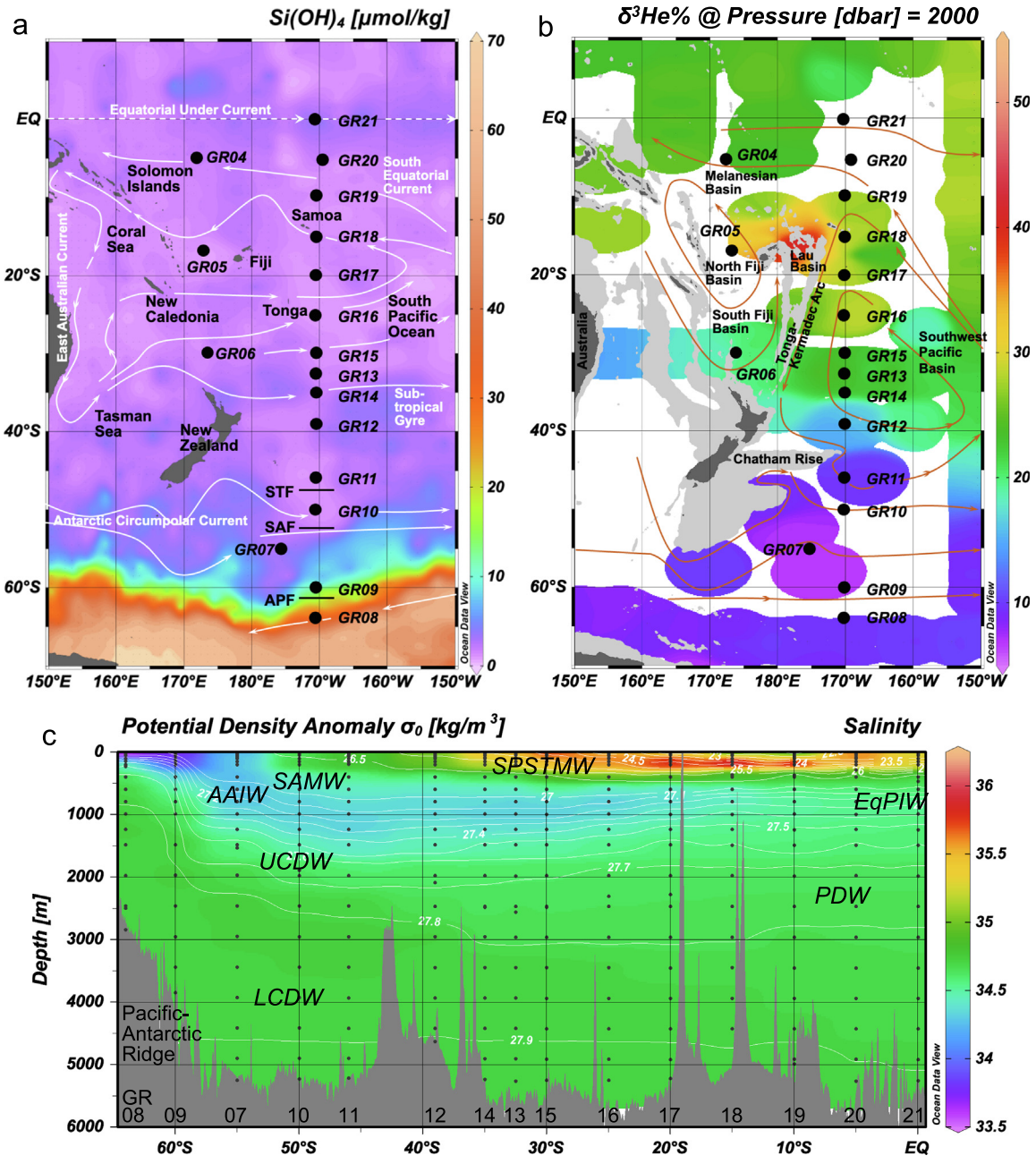

Fig. 1. (a) Map showing the sampling stations in this study. The color contour shows the annually averaged surface $Si(OH)_4$ concentrations from the World Ocean Atlas V2 2013 (www.nodc.noaa.gov). The white lines show geostrophic circulation at the surface (Reid, 1986). STF: Subtropical Front; SAF: Subantarctic Front; APF: Antarctic Polar Front. (b) Map showing the sampling stations in this study. The color contour shows δ^3He at a depth of 2000 m (Jenkins et al., 2019). The red lines show geostrophic circulation at 2000 m depth (Reid, 1986). (c) Sectional distribution of salinity along GP19. The white line contour shows potential density anomaly (σ_0). The black dots show data points. SPSTMW: South Pacific Subtropical Mode Water; SAMW: Subantarctic Mode Water; AAIW: Antarctic Intermediate Water; EqPIW: Equatorial Pacific Intermediate Water; UCDW: Upper Circumpolar Deep Water; PDW: Pacific Deep Water; LCDW: Lower Circumpolar Deep Water. (For interpretation of the references to color in this figure legend, the reader is referred to the web version of this article.)

these water masses (Bostock et al., 2010; Talley et al., 2011) are summarized in Table 1. Detailed descriptions of the water masses were reported in a previous study (Sieber et al., 2019). The GP19 transect exists mostly along the major passage of the LCDW from the Southern Ocean to the North Pacific Ocean (Kawabe and Fujio, 2010; Schlitzer, 2007).

2.2. Sampling and analysis

We collected seawater samples during the Japanese GEOTRACES cruises (KH-14–6) using a clean sampling system (Sohrin and Bruland, 2011). The system was based on a Carousel sampling system (SBE-32, Sea-Bird Scientific, USA) equipped with conductivity, temperature, and depth (CTD) sensors (SBE-9-plus, Sea-Bird Scientific), as well as Niskin-X bottles (General Oceanics, USA). At the beginning of the cruises, the insides of the Niskin bottles were cleaned with 1.5 % detergent, 0.1 mol/kg HCl, and deionized water prepared with a Milli-Q system (MQW; Merck Millipore, Germany). The clean sampling system was deployed using a titanium-armored cable. Seawater samples from layers deeper than 5300 m were collected using a Niskin-X bottle in the different cast with a Kevlar cable. The seawater temperature was measured

Table 1
Summary of water mass data.

Water mass	Latitude	Salinity	Potential Temperature [°C]	σ_θ [kg/m^3]	Reference	Al [nmol/kg]			Mn [nmol/kg]			Co [pmol/kg]			Pb [pmol/kg]		
						td	d	lp	td	d	lp	td	d	lp	td	d	lp
South Pacific Subtropical Mode Water (SPSTMW)	20–40°S	35.5	15–19	26.0	Talley et al. 2011	1.1–5.3	1.0–5.6	ND–0.62	0.45–0.81	0.32–0.77	ND–0.13	8.4–17	5.3–11	ND–7.4	9.2–12	8.4–12	ND
Subantarctic Mode Water (SAMW)	30–55°S	34.4	6–9	26.7–26.9	Talley et al. 2011	0.13–5.1	0.14–3.8	ND–1.4	0.27–0.77	0.17–0.76	ND–0.10	24–36	21–34	ND–4.6	11–14	9.8–14	ND–1.4
Antarctic Intermediate Water (AAIW)		34.1–34.5	4–6	27.0–27.2	Talley et al. 2011	0.50–4.6	0.16–2.9	ND–1.8	0.19–0.44	0.13–0.31	0.05–0.13	29–40	27–36	ND–9.0	8.3–16	6.6–16	ND–1.8
Equatorial Pacific Intermediate Water (EqPIW)		34.5–34.6		27.2–27.4	Bostock et al. 2010	1.3–2.5	1.1–2.2	ND–0.50	0.29–0.41	0.19–0.29	0.07–0.12	28–35	25–35	ND–4.3	8.5–12	7.1–11	ND–1.4
Upper Circumpolar Deep Water (UCDW)		34.6	2–3	27.5–27.7	Talley et al. 2011	0.13–6.1	ND–4.2	ND–2.1	0.22–0.62	0.15–0.42	ND–0.20	20–37	18–35	ND–3.7	4.2–10	4.2–9.4	ND–1.3
Pacific Deep Water (PDW)		34.65–34.69	1–3	27.7–27.8	Talley et al. 2011	1.2–6.0	0.88–3.5	ND–2.5	0.26–0.59	0.19–0.42	0.07–0.19	17–21	15–18	ND–3.7	2.4–5.3	2.1–4.7	ND
Lower Circumpolar Deep Water (LCDW)		> 34.69	< 1	27.8–27.9	Talley et al. 2011	0.80–28	0.31–6.1	ND–26	0.20–1.3	0.12–0.35	ND–1.1	15–28	12–21	ND–15	2.5–7.3	2.2–5.4	ND–4.3

using the CTD sensor. Salinity was determined using a bench salinometer that was standardized based on the IAPSO standard seawater, the O_2 content was measured using the Winkler method, and nutrient ($Si(OH)_4$, NO_3, NO_2, and PO_4) concentrations were determined by spectrophotometry using an automated analyzer onboard the vessel. Algal chlorophyl *a* (Chl. *a*) was collected on a Whatman GF/F glass fiber filter and measured by fluorometry. We performed these measurements in accordance with the protocols for the Joint Global Ocean Flux Study (JGOFS) (Knap et al., 1996). The nutrient determination was calibrated using the reference material for nutrients in seawater (KANSO, Japan).

The Niskin-X bottles were placed into a clean bubble immediately after sampling. Seawater samples for dissolved metal (dM) analysis were filtered through an AcroPak 200 capsule filter with a pore size of 0.8/0.2 μm (Pall, USA), collected in precleaned Nalgene low-density polyethylene (LDPE) bottles (Thermo Fisher Scientific, USA), and acidified to be 0.02 mol/kg HCl (Tamapure AA-10, Tama Chemicals, Japan or Optima, Thermo Fisher Scientific). A portion of the seawater sample for total dissolvable metal (tdM) analysis was directly collected in an LDPE bottle and acidified in a similar manner. These samples were stored at ambient temperature for several years prior to the analysis.

An off-line automated solid-phase extraction system (SPE-100, Hiranuma Sangyo, Japan) equipped with a column of Nobias Chelate-PA1 resin (Hitachi High Technologies, Japan) was used for the preconcentration of Al, Mn, iron (Fe), Co, nickel (Ni), copper (Cu), zinc (Zn), cadmium (Cd), and Pb from seawater samples (Minami et al., 2015). The seawater samples were adjusted to pH 6.00 ± 0.05, just before preconcentration by adding an acetic acid (HAcO)–ammonium acetate (NH_4AcO) buffer solution prepared from ultrapure HAcO (Optima) and NH_3 (TAMAPURE AA-10). When preconcentrating the tdM species, unfiltered samples were first passed through a Millex syringe filter with a pore size of 0.45 μm (Merck Millipore) and then introduced into the SPE-100. The nine metals were eluted with 1.0 mol/kg HNO_3 (Optima) and determined with a high-resolution inductively coupled plasma mass spectrometer (HR-ICP-MS, Element 2, Thermo Fisher Scientific) using calibration curves. The exact concentration factor was calculated based on the weights. Although data of lpFe are used in this paper for discussion, the detailed results of Fe, Ni, Cu, Zn, and Cd will be reported in a forthcoming paper.

We evaluated the procedure blanks using the MQW as a sample. The MQW was initially acidified with HCl and then adjusted to pH 6.00 for preconcentration, which was a process similar to that used for seawater samples. We defined the detection limits for tdM and dM as three times the standard deviation (sd) of the procedure blank. The labile particulate metal (lpM) concentrations were obtained by taking the difference between tdM and dM. As discussed in our previous paper (Zheng et al., 2019), the concentrations of lpM were comparable with those of metals collected on a membrane filter. Thus, lpM represents a major fraction of suspended particulate metals which are contained in aluminosilicates, Fe-Mn oxyhydroxides, and biogenic particles. Because the relative standard deviation (rsd) for replicate analysis of the same sample was ~ 5 % for both tdM and dM at average seawater concentrations for all metals, the detection limit of lpM was defined as two times the propagated uncertainty: $2 \times \sqrt{2} \times 0.05 \times C_{ave}$, where C_{ave} represents the average concentration of each dM in this study. The procedure blanks, detection limits, and numbers of samples of KH-14–6 are summarized in Supplementary Table 1. We measured the certified reference materials for trace metals, CASS-5 and NASS-6 (National Research Council Canada), and GEOTRACES open-ocean reference samples SAFe-D2, GS, and GD at an early point in the study (Minami et al., 2015). We participated in the intercalibration campaign of new reference materials of CASS-6

and NASS-7, contributing to the establishment of certified values later in the study (Yang et al., 2018). Recently, we measured new GEOTRACES reference samples, GSP, and GSC1. All of these data confirmed the accuracy of the trace metal data in this study (Supplementary Table 2). Some of our data (dAl, dMn, dCo, and dPb) were intercalibrated at crossover stations GR6 and GR13 with data from the GEOTRACES GP13 transect and adopted in the GEOTRACES Intermediate Data Product 2021 (IDP2021; https://www.geotraces.org/geotraces-intermediate-data-product-2021/).

As described in the introduction, we refrained from using UV irradiation to minimize possible contamination of the nine metals and to avoid unknown effects of UV irradiation on the determination of the nine metals (Wuttig et al., 2019; Zheng et al., 2017). Thus, it should be noted that our Co data are operational results and have not been included in the IDP2021. However, the UV-dCo data from the GPc03 transect (Hawco et al., 2020) are contained in the IDP2021. Because station 10 of GPc03 was located at the same position as our station GR18, we compared the profiles of the UV-dCo and our non-UV-dCo (Supplementary Fig. 1). This was the first crossover station between UV-dCo and our non-UV-dCo. Although the non-UV-dCo accounted for approximately 64 % of the UV-dCo at this station, the profile of non-UV-dCo fluctuated less than that of UV-dCo. This result implies that non-UV-dCo represents a labile portion of total dCo that is measured as UV-dCo. However, the profiles of our non-UV-dCo at the crossover stations GR6 and GR13 are consistent with those of non-UV-dCo determined by Australia and New Zealand scientists, suggesting that non-UV-dCo can be measured with high reproducibility. Therefore, we believe our Co data, as well as those of the other elements, are valuable for oceanographic discussions.

3. Results

Seawater data are summarized in Supplementary Table 3. ND represents the data less than the detection limits. For tdM and dM, several samples were ND only for Al (Supplementary Table 1). For lpM, the percentage of ND was 46 % for lpAl, 21 % for lpMn, 60 % for lpCo, and 89 % for lpPb. Thus, distribution figures are not shown for lpPb below. The highest lpPb of ~ 8 pmol/kg in surface water was observed at GR18, and the highest lpPb of ~ 4 pmol/kg in the bottom water was observed at GR07.

The sectional distributions of dAl, dMn, dCo, dPb, lpAl, lpMn, and lpCo along the GP19 section are shown in Fig. 2. It is apparent that dAl, dMn, dCo, and dPb show different distribution from each other. The dAl concentration to the south of the SAF (~47°S) was<1.2 nmol/kg (Fig. 2a), which is consistent with the data from the GIPY06 section situated to the south of Tasmania (Remenyi et al., 2012). Some dAl maxima were observed on the GP19 section. A dAl maximum of ~ 7 nmol/kg occurred in the EUC at 200 m depth on the equator. Dissolved Al showed a surface maximum between 20°S and 30°S, an intermediate depth (~2000 m) maximum between 10°S and 40°S, and a near-bottom maximum between 10°S and 35°S. Dissolved Mn showed a broad maximum between 50°S and the equator from the surface to a depth of 200 m (Fig. 2b). The highest dMn concentration of ~ 1 nmol/kg occurred in surface water at GR16, where the dAl concentration was also high. A mid depth maximum of dMn occurred in a depth range of 800–3500 m between 25°S and 15°S. The concentrations and vertical profiles of dMn in this study are consistent with those observed in the equatorial Pacific Ocean (Chen and Wu, 2019). In contrast to dMn, dCo was depleted in surface water between 5°S and 35°S (Fig. 2c). The dCo concentration in the surface water increased southward, which reached ~ 28 pmol/kg around the APF. The highest dCo concentration occurred around a potential density anomaly (σ_θ) ~ 27.0, where the AAIW flows. A similar distribution of dCo was observed near Tasmania (Butler et al., 2013; Ellwood, 2008) and in the southeastern Atlantic Ocean and the Southern Ocean (Bown et al., 2011). The enrichment of dCo was also observed in EqPIW to the north of 5°S (Fig. 2c). The dPb concentration in surface water was as high as ~ 21 pmol/kg on the equator and decreased southward (Fig. 2d). The highest dPb concentration occurred in the Equatorial Intermediate Current (EIC) at a depth of ~ 300 m on the equator. Dissolved Pb exhibited a maximum at σ_θ approximately 26.9, where SAMW exists. Although the maximum depth was slightly shallower for dPb than for dCo, the similar distributions of both elements in deep water (>1500 m) imply control by the same mechanism. Generally, the concentrations and vertical profiles of dPb are consistent with those observed in the Tasman Sea (Ellwood, 2008) and the South Pacific Ocean (Boyle et al., 2020; Pinedo-González et al., 2018; Wu et al., 2010).

Labile particulate Al, lpMn, and lpCo show similar distribution along GP19. The sectional distribution of lpAl along GP19 (Fig. 2e) is totally different from that of dAl. A strong near-bottom maximum of up to ~ 28 nmol/kg occurred between 55°S and 39°S, where the LCDW flows down from the Pacific-Antarctic Ridge. The distribution of lpMn was similar to that of lpAl (Fig. 2f). There was a linear relationship between lpMn and lpAl in the western South Pacific (64°S–0°S) with a type II regression (Supplementary Fig. 2):

$$\mathrm{lpMn\,[nmol/kg]} = 0.0437\,\mathrm{lpAl\,[nmol/kg]} + 0.10 \quad (1)$$

$$R^2 = 0.752, n = 188$$

The slope was approximately 10 times higher than the Mn to Al ratio of 4.7×10^{-3} in the upper crust (Rudnick and Gao, 2005). Significantly higher lpMn than this regression occurred above bottoms at GR05, GR06, and GR16. Although lpCo was detected in 40 % of the total samples and was not detected for the other samples, the data enabled us to provide a schematic view of the sectional distribution of lpCo along GP19 (Fig. 2g). In contrast to lpAl and lpMn, lpCo showed surface maxima in 64°S–60°S, 50°S–46°S, and 5°S–0°S. The surface lpCo probably represents Co incorporated by phytoplankton and cyanobacteria. It should be noted that the lpCo concentration was low between 35°S and 5°S, where dCo was depleted. In the deep water, the distribution of lpCo resembled that of lpAl, suggesting the dominance of lithogenic particles. The concentration ranges of each element in water masses are summarized in Table 1.

The vertical profiles are compared in Fig. 3 for dAl, lpAl, dMn, lpMn, dCo, and dPb between stations along ~ 174°E and ~ 170°W in the western South Pacific. The distances between western and eastern stations are 2000–1540 km. The dAl concentrations were high in surface water at GR05, GR06, and GR15 (Fig. 3a). The dAl concentrations were also high in bottom waters at GR05 and GR06 in the Fiji Basins. The lpAl concentrations generally increased with depth at GR05, although they showed minima at a depth of ~ 2000 m and near-bottom maxima at the other stations (Fig. 3b). The surface concentration of dMn reached 1.3 nmol/kg at GR05 and GR06 in the Fiji Basins (Fig. 3c). A strong dMn maximum of ~ 4.7 nmol/kg occurred at a depth of 1938 m at GR05. The lpMn concentrations were significantly higher at stations near the Lau Basin and in the Fiji Basins (Fig. 3d). In contrast, the vertical profiles of dCo and dPb were generally similar among the six stations (Fig. 3e, f). However, relatively high dCo concentrations were observed at a depth range of 200–800 m at GR04 and 20. The dPb concentrations in surface water decreased from northern stations to the southern stations.

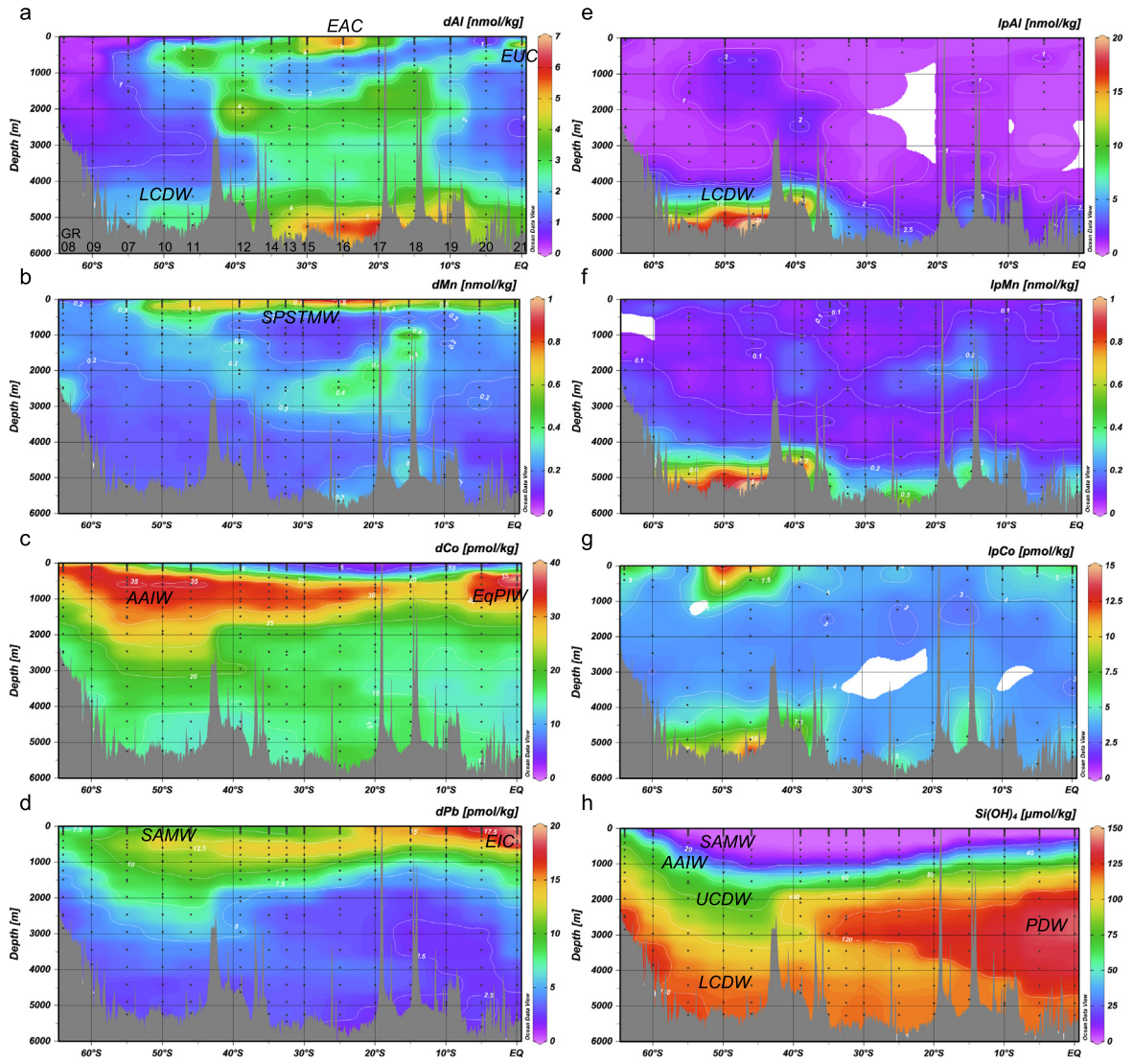

Fig. 2. Full-depth sectional distribution of (a) dAl, (b) dMn, (c) dCo, (d) dPb, (e) lpAl, (f) lpMn, (g) lpCo, and (h) $Si(OH)_4$ along GP19. EAC: East Australian Current; EUC: Equatorial Under Current; LCDW: Lower Circumpolar Deep Water; SPSTMW: South Pacific Subtropical Mode Water; AAIW: Antarctic Intermediate Water; EqPIW: Equatorial Pacific Intermediate Water; SAMW: Subantarctic Mode Water; EIC: Equatorial Intermediate Current; UCDW: Upper Circumpolar Deep Water; PDW: Pacific Deep Water.

4. Discussion

4.1. Lithogenic and hydrothermal sources in the western South Pacific

The data in this study show that dAl is generally transported from west to east (Fig. 3). Dissolved and particulate Al are transported eastward by the EUC from the northeastern coastal margins of New Guinea and New Ireland (Kaupp et al., 2011; Slemons et al., 2012). This feature was ascertained in the GP19 section in this study and in the GPc06 section at 160°W (Zheng et al., 2019). The vertical profiles of dAl at GR05 and GR06 in the Fiji Basins exhibited substantially elevated concentrations particularly in the surface and bottom waters (Fig. 3a). The observed surface maxima are probably owing to the supply of dAl from the surrounding islands, and the bottom maxima are ascribed to the dissolution of dAl from the sediments. The vertical profiles of dAl at GR15 and GR18 imply the transport of dAl from the Fiji Basins to the Southwest Pacific Basin. The maximum dAl at ~ 400 m depth, 45°S on the GP19 section is attributed to the supply of dAl from the Chatham Rise (Fig. 2a). The LCDW flows from the south to the north below a depth of 4000 m, where dAl did not exhibit a gradual trend. A broad maximum occurred between 32°S and 10°S, and elevated dAl concentrations up to ~ 6 nmol/kg were observed near Tonga and Samoa. These results suggest that terrigenous materials supplied from neighboring islands deposit at the bottom and release dAl.

Because there were not available δ^3He data during the KH-14–6 cruise, we compared the vertical profiles of dMn and lpMn at some stations in this study with those of δ^3He at near stations (Jenkins et al., 2019) (Supplementary Fig. 3). The near-bottom anomalies in dMn and lpMn at GR05 in the North Fiji Basin were accompanied with an anomaly in δ^3He, suggesting that they were caused by a hydrothermal input. In a previous study, Mn and methane anomalies were observed in this area, which were ascribed to hydrothermal plumes from a hydrothermal system on the North Fiji Basin triple junction (Sedwick et al., 1990). The ratio of tdMn : excess ^{3}He (Jenkins et al., 2020) was estimated to be approximately 7×10^6 for the near-bottom anomaly at GR05. The ratio was ND–336×10^6 for hydrothermal plumes from a 2008 submarine eruption on the Northeast Lau Spreading Center (Baumberger et al., 2020) and ND–8×10^6 for plumes from the northeast Lua Basin into the southwest Pacific (Cohen et al., 2021). At GR15

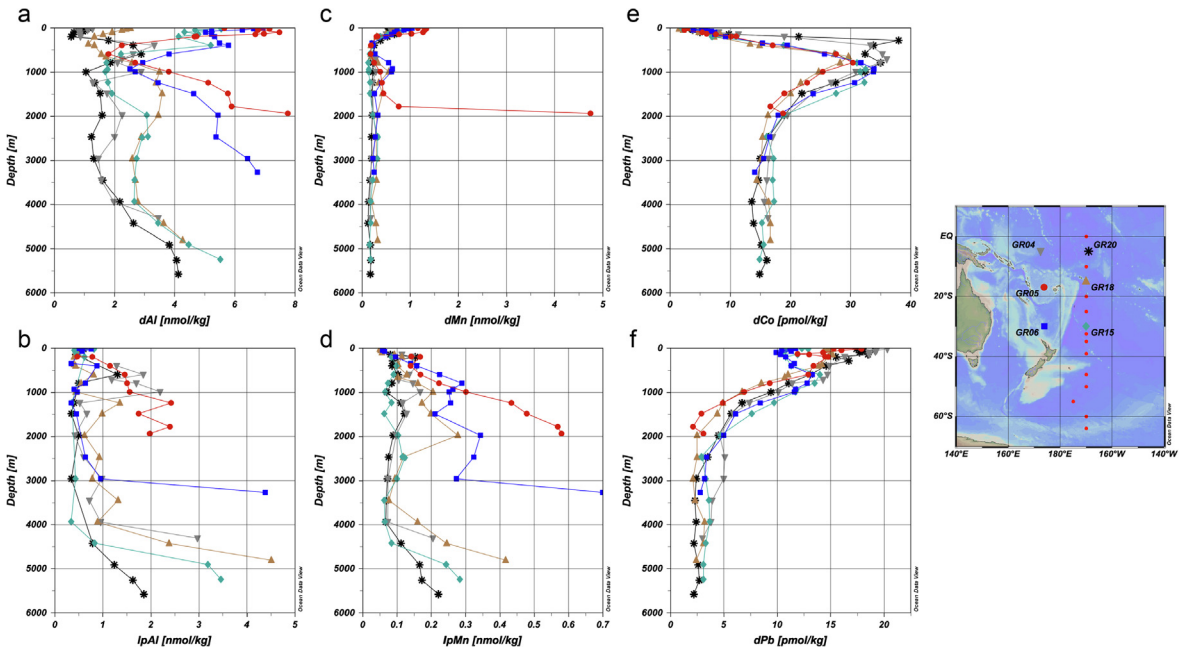

Fig. 3. Vertical profiles of (a) dAl, (b) lpAl, (c) dMn, (d) lpMn, (e) dCo, and (f) dPb at GR04 (grey inverted triangles), GR05 (red circles), GR06 (blue squares), GR15 (cyan diamonds), GR18 (brown triangles), and GR20 (black asterisks). (For interpretation of the references to color in this figure legend, the reader is referred to the web version of this article.)

and 18, there were broad maxima of dMn and lpMn in a depth range of 1000–3500 m, which were accompanied with maxima of δ^3He (Supplementary Fig. 3b, c). Although the tdMn : excess ^{3}He ratio was approximately 5 × 10^5 for the peaks of δ^3He at a depth of 2500 m, it is probable that hydrothermal inputs from the Lau Basin and the Tonga-Kermadec Arc contributes to the mid depth maximum of dMn in a depth range of 800–3500 m between 25°S and 15°S along GP19 (Fig. 2b). In bottom water at GR08 above the Pacific-Antarctic Ridge, the dMn concentrations were slightly elevated, which is also likely because of hydrothermal activity.

In surface water, the dMn concentrations were high at GR05, GR06, and GR15 in a similar manner to dAl (Fig. 3b, a). Thus, lithogenic sources have significant effects on the distribution of dMn in this area. At GR06, the vertical profile of dMn was decoupled from that of δ^3He (Supplementary Fig. 3d), implying a minor effect of hydrothermal activity on dMn. Along GP19, the sectional distribution of dMn showed a similarity with that of dAl in a depth range of 500–3000 m between 50°S and 10°S (Fig. 2b, a). The regression line between dMn and dAl was as follows:

$$\mathrm{dMn\,[nmol/kg]} = 0.0650\,\mathrm{dAl\,[nmol/kg]} + 0.10 \qquad (2)$$

$$R^2 = 0.418,\ n = 111$$

This moderate correlation suggests that lithogenic inputs from the Chatham Rise, the Fiji Basins, and the Tonga- Kermadec Arc have some effects on the distribution of dMn along GP19.

The vertical profiles of dCo and dPb at GR05 and GR06 were similar to those at GR15 and GR18 (Fig. 3e, f), which indicates that local sources, such as islands, terrigenous sediments, and hydrothermal sites, have insignificant effects on dCo and dPb.

4.2. Interplay between the South and North Pacific

The results from the South Pacific in this study were combined with those from the North Pacific in our previous study (Zheng et al., 2017) to investigate the whole basin scale characteristics in the Pacific Ocean. The vertical profiles of dM and lpM were compared between the station GR21 (170°W, 0°N) on GP19 section and the station ST03 (160°W, 0°N) on GPc06 section in Supplementary Fig. 4. Although these stations were away by ∼ 1120 km and the sampling times were apart by 9 years, the profiles were similar to each other. The largest offset in deep water concentrations between the two stations was observed for dPb. It was approximately 8 pmol/kg, which may have been caused by a systematic error in analysis. We have used the data of GP19 and GPc06 to obtain meridional sections of dM and lpM from 64°S to 53.6°N. Both the data from GR21 and GP19 were merged in these sections. We do not think this processing caused a significant artifact.

4.2.1. Aluminum

Fig. 4 shows the sectional distributions of dAl and lpAl along GP19 (170°W) in the South Pacific and GPc06 (160°W) in the North Pacific. To the best of our knowledge, these are the first full-basin scale distributions of dissolved and suspended particulate species of Al in the Pacific Ocean. Obviously, the sectional distributions are totally different between dAl and lpAl. Concerning dAl, strong sources were present in the South Pacific (Fig. 4a). For example, dAl showed a maximum between 40°S and 15°S at a depth of 2000 m. Fig. 5 shows the distributions of dAl and lpAl at the surface (∼10 m depth), 1938 m depth (the deepest sampling depth at GR05), and 4500 m depth. The data from the East China Sea, Japan Sea, and Okhotsk Sea (Nakaguchi et al., 2021; Nakaguchi et al., 2022) are also shown in Fig. 5. The dAl concentration in surface water was high between 35°S and 10°S and between 5°S and 30°N (Fig. 5a). In particular, high dAl occurred in the Fiji Basins, near Hawaii, and in the East China Sea. At a depth of 1938 m, the Fiji Basins were the strongest source of dAl (Fig. 5c). At a depth of 4500 m, dAl in deep water is generally transported from south to north by the LCDW; nonetheless we observed local maxima near Tonga, Samoa, and Hawaii Islands (Fig. 5e). Latitudinal distribution of dAl for all samples showed a maximum between 30°S and 0°S (Supplementary Fig. 5a). Previous studies have suggested that the primary source of dAl to the ocean is dust deposition (Measures

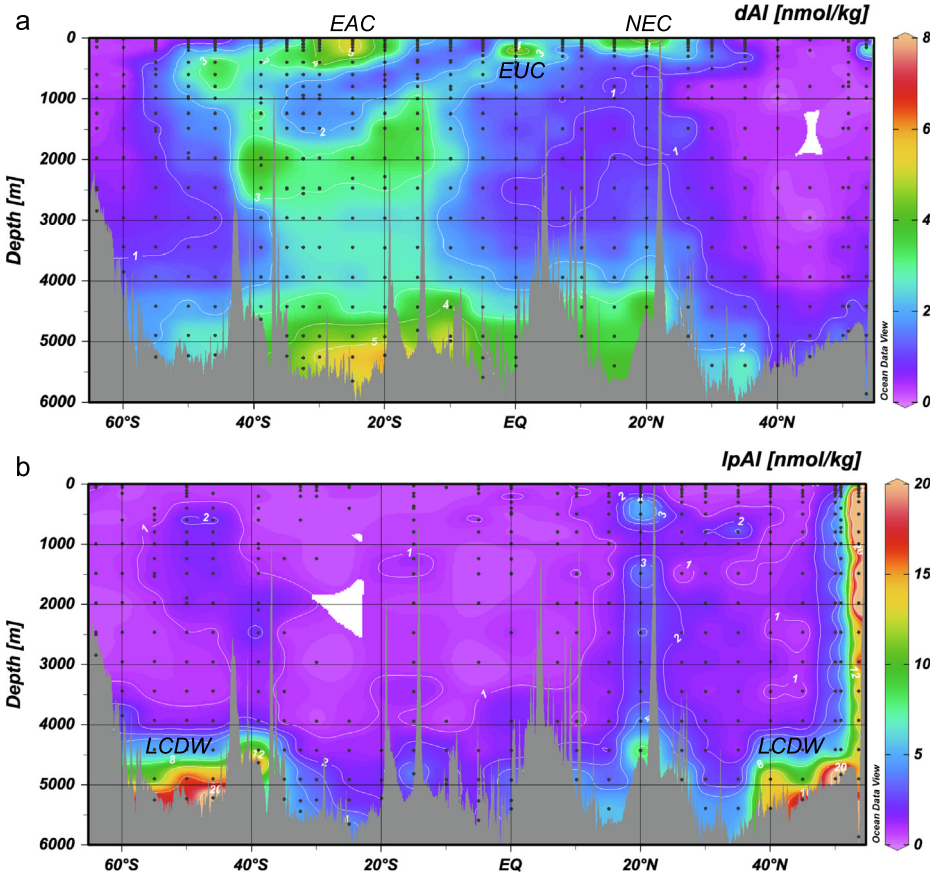

Fig. 4. Full-depth sectional distribution of (a) dAl and (b) lpAl along GP19 (170°W) in the South Pacific and GPc06 (160°W) in the North Pacific. The data for the North Pacific were acquired from (Zheng et al., 2019). EAC: East Australian Current; EUC: Equatorial Under Current; NEC: North Equatorial Current; LCDW: Lower Circumpolar Deep Water.

and Vink, 2000; van Hulten et al., 2014). Observational and modeled dust deposition is higher between 20°N and 50°N than that to the south of 20°N in the Pacific Ocean (Buck et al., 2013; Zhang et al., 2015). However, it is difficult to explain the latitudinal distribution of dAl in the Pacific Ocean based on dust deposition. In addition, a strong source of lpAl is the continental shelf and slope near the Aleutian Islands (Fig. 4b, 5b, 5d). The high lpAl concentration in bottom water occurred to the south of 40°S and to the north of 40°N (Fig. 4b, 5f). Latitudinal distribution of lpAl for all samples showed a maximum between 60°S and 30°S and to the north of 40°N (Supplementary Fig. 5b). These distributions cannot be explained by dust deposition.

We point out that the distribution of Al in the Pacific Ocean is characterized by the distribution of the lpAl/tdAl ratio with the latitude (Fig. 6a). The vertical distribution of the lpAl/tdAl ratio is shown in Supplementary Fig. 6a. Overall the lpAl/tdAl ratio was 0.62 ± 0.23 (ave ± sd, n = 645) in the Pacific Ocean, indicating the dominance of particulate species. However, the lpAl/tdAl ratio had a minimum of 0.26 ± 0.12 (n = 116) in the zone between 30°S and 0°S. This result implies a high dAl flux in this zone and the supply of mineral particles that easily release dAl. Intensive weathering releases Al and Fe from the bedrock to form kaolinite-dominated soils and laterites in tropical and subtropical zones (Brimhall et al., 1991). Laterites are residual surficial accumulations of insoluble oxides and hydrous oxides of Al, Fe, and other metals. It is likely that a part of the released Al and Fe finds a way into the ocean through runoff, rivers, and groundwater. Under prevailing acidic conditions in the kaolinite-dominated soils, kaolinite dissolution occurs, contributing to high levels of soluble Al in these soils (Khawmee et al., 2013). It has been suggested that the weathering of islands in the western equatorial Pacific, such as Papua New Guinea, is a major source of Al, Fe, and rare earth elements to the Pacific Ocean (Milliman et al., 1999; Sholkovitz et al., 1999). Thus, we propose that surface and subsurface currents carry dAl from the tropical and subtropical islands, which has a dominant effect on the distribution of dAl in the surface water of the Pacific Ocean. The effect of currents on the distribution of dAl has been suggested in the Atlantic Ocean (Menzel Barraqueta et al., 2019; Middag et al., 2015) and in the Indian Ocean (Vu and Sohrin, 2013).

Previous studies have suggested that resuspension of sediments is the major mechanism for the near-bottom maximum of dAl in the Atlantic (van Hulten et al., 2014). The near-bottom maxima of lpAl should reflect intense resuspension to the south of 40°S and to the north of 40°N in the Pacific Ocean (Fig. 4b). However, the maxima of dAl do not coincide with those of lpAl (Fig. 4a), suggesting that the intensity of resuspension is not a dominant factor controlling the distribution of dAl in the bottom water; rather, we propose that the nature of the sediments is a key factor. Because Al is supplied to the ocean extensively by clay particles, the distribution of clay minerals is important. Chlorite is the dominant mineral in the < 2 μm size fraction of sediments south of 40°S and north of 40°N in the Pacific Ocean (Griffin et al., 1968). However, kaolinite is dominant between 30°S and the equator in the western South Pacific (Griffin et al., 1968). The kaolinite-dominated sediments are derived from Australia and islands, spreading in the Fiji Basins and the Southwest Pacific Basin (Brimhall et al., 1991). Experiments shown that kaolinite promptly releases dAl at pH 1–4 (Khawmee et al., 2013). We suppose that kaolinite in sediments has a relatively high dissolution

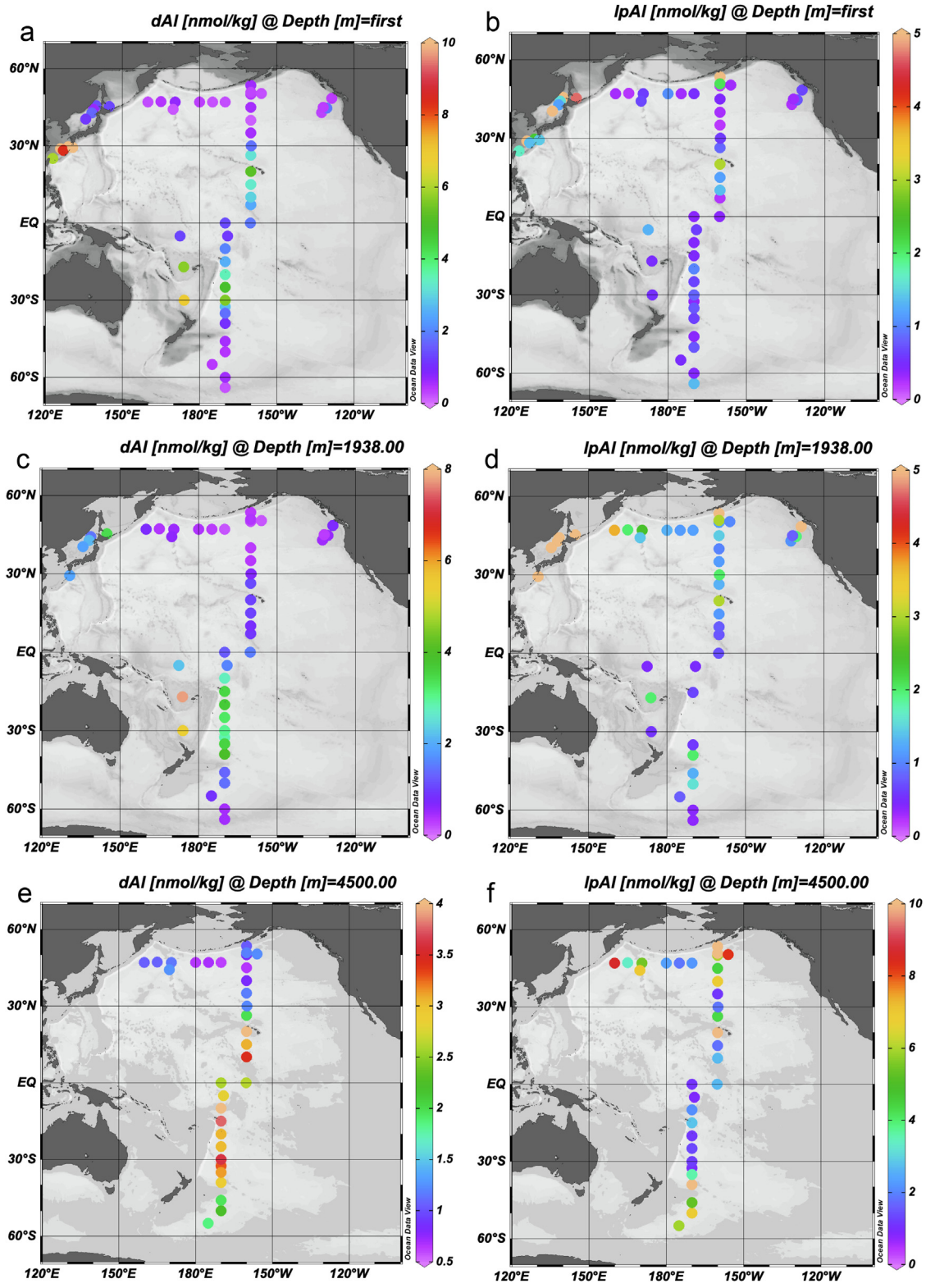

Fig. 5. Horizontal distribution of (a) dAl and (b) lpAl at the surface (~10 m depth), (c) dAl and (d) lpAl at a depth of 1938 m depth, and (e) dAl and (f) lpAl at a depth of 4500 m. The data for the North Pacific, the East China Sea, and the Japan and Okhotsk Seas were acquired from (Zheng et al., 2019), (Nakaguchi et al., 2021), and (Nakaguchi et al., 2022), respectively.

rate of dAl even under basic conditions in seawater as well as under acidic conditions. Thus, the supply of kaolinite from Australia and the islands should be a predominant factor controlling the distribution of dAl in the deep waters of the Pacific Ocean. In addition, Tonga, Samoa, and Hawaii are volcanic islands composed mainly of basalts and other volcanic products. Detritus basalts deposit around these islands and probably release dAl by low-temperature alteration during seafloor weathering (Pichler et al., 1999). This effect is superimposed to produce the strongest dAl maxima in the bottom water.

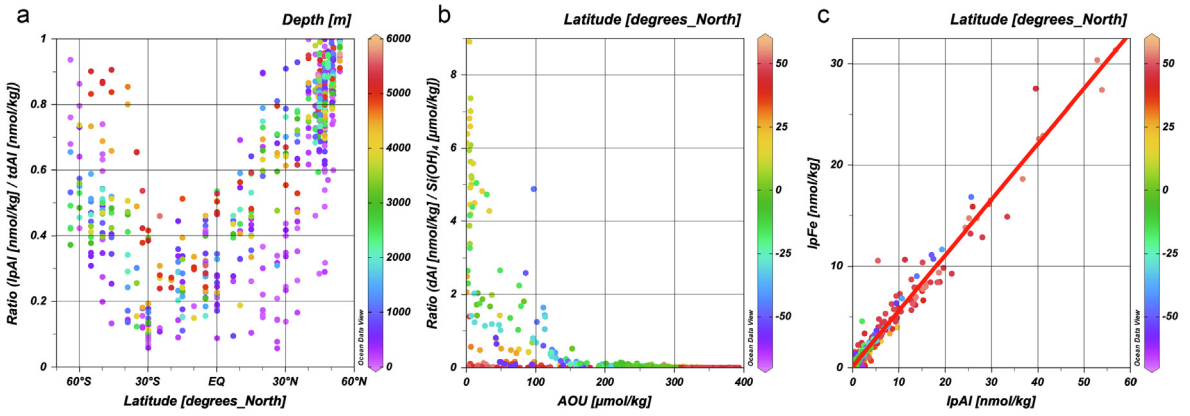

Fig. 6. (a) lpAl/tdAl ratio against the latitude for all samples in the Pacific Ocean. The dot color shows the depth. (b) dAl/Si(OH)$_4$ ratio ($\times 10^{-3}$) against AOU. The dot color shows the latitude. (c) lpFe vs lpAl. The red line is the regression line mentioned in the text. The dot color shows the latitude. (For interpretation of the references to color in this figure legend, the reader is referred to the web version of this article.)

In the North Atlantic Ocean, dAl exhibits a linear relationship with Si(OH)$_4$ (Middag et al., 2015). Based on this and other observations, biogenic silica particles have been thought to play a major role in Al cycling in the ocean (van Hulten et al., 2014). However, this correlation was not observed in the Pacific Ocean (Supplementary Fig. 5c) similar to observations in the Southern Ocean (Middag et al., 2011; Middag et al., 2012). The dAl/Si(OH)$_4$ ratio strongly decreased with an increase in the AOU in the Pacific Ocean (Fig. 6b), implying that dAl is preferentially scavenged from seawater with time. The Al/Si(OH)$_4$ ratio was (0.015 ± 0.020) × 10^{-3} (n = 499) at a depth below 2000 m (AOU > 138), which is much lower than the Al/Si ratio in diatoms of ∼ 10^{-3} (Gehlen et al., 2002; Koning et al., 2002), indicating that the preferential scavenging of dAl has an overwhelming effect on the distribution of dAl. Throughout the Pacific Ocean, lpAl showed a strong linear relationship with lpFe (Fig. 6c):

$$\mathrm{lpFe\,[nmol/kg]} = 0.549\,\mathrm{lpAl\,[nmol/kg]} + 0.1 \quad (3)$$

$$R^2 = 0.966,\ n = 627$$

This remarkable relationship suggests that dAl is concurrently scavenged with dFe. These results imply that lithogenic aluminosilicate particles serve as a major substrate, on which authigenic Fe-Mn oxyhydroxide is formed. Then the Fe-Mn oxyhydroxide surface works as strong scavenger of dAl. It is unlikely that biogenic silica particles have a major effect on the distribution of dAl and lpAl in the Pacific Ocean.

4.2.2. Manganese and cobalt

The sectional distributions of dMn and lpMn from the South Pacific to the North Pacific are shown in Fig. 7a and Supplementary Fig. 7a, respectively. A characteristic of dMn was the board surface maximum to the north of 50°S. The surface maximum of dMn is owing to the dissolution of dMn from deposited dust (Buck et al., 2013) and to the photoreduction of manganese oxides that are supplied by dust deposition (Sunda and Huntsman, 1994). Labile particulate Mn did not show the surface maximum, suggesting that the resolution is a fast reaction. Both dMn and lpMn showed that the strongest source in the Pacific Ocean is the continental shelf along the Aleutian Islands, which is attributed to manganese reduction in sediments (Zheng et al., 2019). The hydrothermal activities in the Southern Pacific are a minor source for dMn. Although lpMn showed a similar distribution with lpAl, a characteristic of lpMn was a near-bottom maximum between 30°S and 10°N (Supplementary Fig. 7a). This is probably attributed to volcanic and hydrothermal activities in this area. The vertical distribution of the lpMn/tdMn ratio is shown in Supplementary Fig. 6b. Overall the lpMn/tdMn ratio was 0.35 ± 0.19 (n = 730) in the Pacific Ocean. Although the ratio did not show variations depending on latitude, it showed an increasing trend with depth. This is likely due to strong scavenging of dMn throughout the water column.

The sectional distributions of dCo and lpCo from the South Pacific to the North Pacific are shown in Fig. 7b and Supplementary Fig. 7b, respectively. In contrast to dMn, dCo was depleted in surface water between 40°S and 40°N. Labile particulate Co showed surface maxima to the south of 40°S, between 5°S and 5°N, and to the north of 40°N. The lpCo showed a moderate correlation with Chl. *a* in the surface mixed layer (<60 m depth) in the Pacific Ocean (Supplementary Fig. 8). These features are ascribed to the uptake of dCo by phytoplankton and cyanobacteria (Hawco et al., 2018; Hawco et al., 2020).

Fig. 7b and Supplementary Fig. 7b show that dCo and lpCo are supplied from the continental shelf sources in a similar manner to dMn and lpMn. The concurrent supply of Mn and Co from manganese reduction in sediments was observed on the Bering Sea shelf (Cid et al., 2011) and in the Chukchi and Beaufort Seas (Cid et al., 2012) and many other regions around the world. The dCo maximum at each station occurred in a σ_θ range of 23.9–27.4 (a depth range of 10–991 m) in the Pacific Ocean. Namely, dCo is concentrated in the North Pacific Intermediate Water (NPIW), EqPIW, and AAIW and spreads throughout the Pacific Ocean, showing a necklace-like maximum on the section (Fig. 7b). The dCo concentration was 23–59 pmol/kg at σ_θ = 27.0 (a depth range of 36–794 m) throughout the Pacific Ocean (Fig. 8a). In contrast, the dMn concentration exhibited a maximum of 1.7 nmol/kg off the Kamchatka Peninsula and decreased to a minimum of 0.08 nmol/kg around the APF on the isopycnal surface of σ_θ = 27.0 (Supplementary Fig. 9a). The limited spreading of dMn is ascribed to the oxidative scavenging of dMn (Moffett and Ho, 1996; von Langen et al., 1997).

The dCo maximum in intermediate water is attributed to three mechanisms. First, dCo is scavenged from seawater. Scavenging of dCo is particularly apparent below the intermediate waters. Second, although dCo is oxidized via a common microbially catalyzed pathway with dMn, the oxidation rate of dCo is ∼ 10 times lower than that of dMn (Moffett and Ho, 1996; von Langen et al., 1997), resulting in a longer residence time in seawater. Thus, dCo supplied from the northern continental shelf is transported through a much longer distance than dMn (Zheng et al., 2019).

Third, dCo is taken up by phytoplankton from surface water, transported downward as biogenic particles, and redissolved by bacterial activity. It is likely that only a small fraction of dMn in

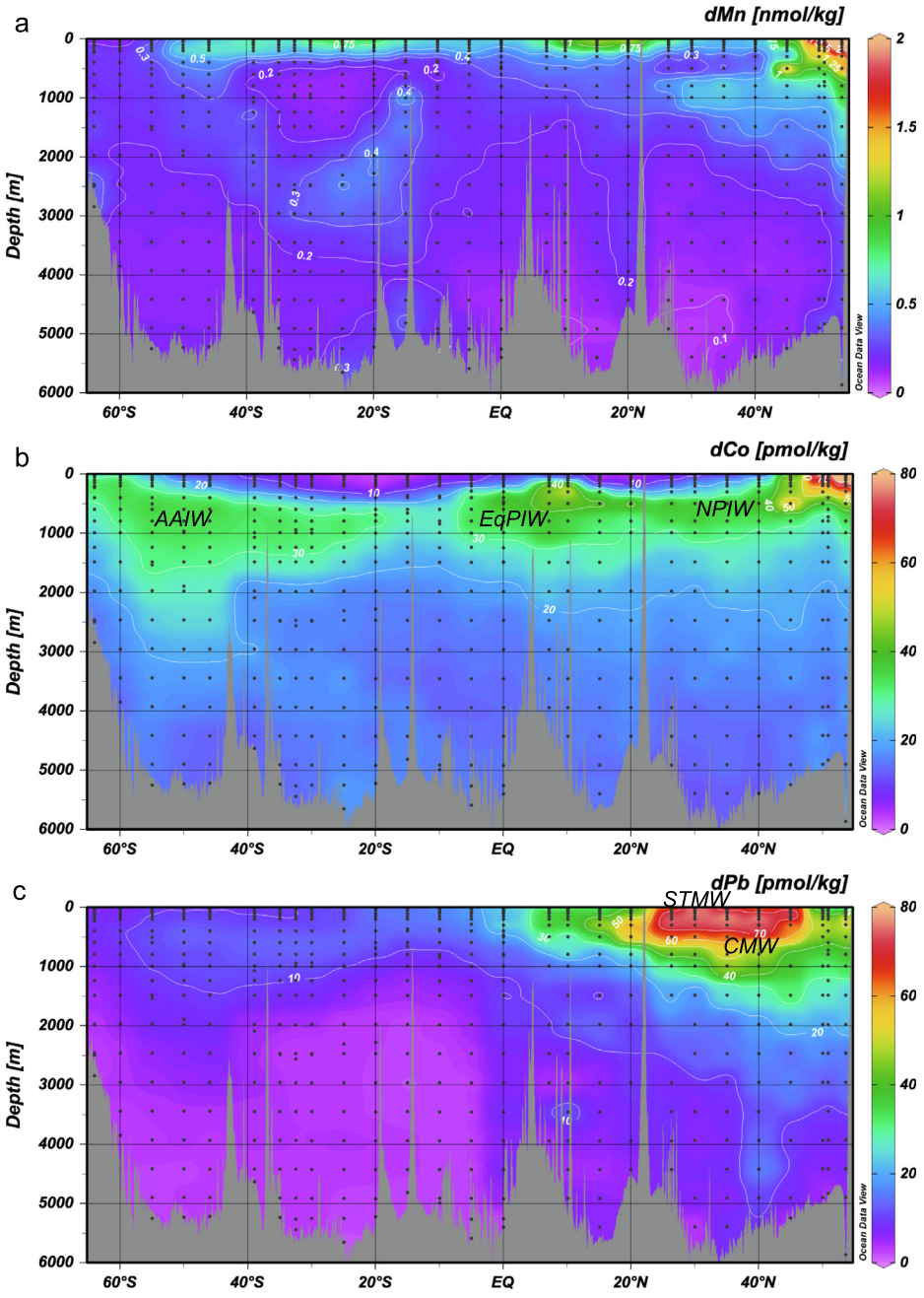

Fig. 7. Full-depth sectional distribution of (a) dMn, (b) dCo, and (c) dPb along GP19 (170°W) in the South Pacific and GPc06 (160°W) in the North Pacific. The data for the North Pacific were acquired from (Zheng et al., 2019). AAIW: Antarctic Intermediate Water; EqPIW: Equatorial Pacific Intermediate Water; North Pacific Intermediate Water; STMW; Subtropical Mode Water; CMW: Central Mode Water.

surface water is involved in this mechanism. A correlation between UV-dCo and PO_4 in the upper water has been reported (Chmiel et al., 2021; Hawco et al., 2018). Our data show that non-UV-dCo was also correlated with PO_4 in upper water (σ_0 < 27.0) (Fig. 9). Relatively high dCo occurred in surface water at northern stations, where dCo is supplied from the continental shelf. The strongest linear relationship between dCo and PO_4 was observed at southern stations between 25°S and 0°S:

$$\mathrm{dCo\,[pmol/kg]} = 14.6\,\mathrm{PO_4\,[\mu mol/kg]} + 0.6 \quad (4)$$

$$R^2 = 0.876,\ n = 77$$

This slope was approximately 40 % of that observed in the North Pacific (Zheng et al., 2019), because the major source of dCo is the continental shelf in the North Pacific. In contrast, dMn did not significantly correlate with PO_4. The uptake of dCo by phytoplankton resulted in an increase in the lpCo/tdCo ratio in the surface water (Supplementary Fig. 6c). The distribution of dCo in the Southern Ocean and South Pacific Ocean also supports the concurrent behavior among Co and nutrients. The PDW mixes with the UCDW and upwells to the sea surface in the Antarctic Zone to the south of the APF (Talley, 2013). Nutrients such as $Si(OH)_4$ return from deep waters by this upwelling and are subsequently entrained into the SAMW and AAIW (Sarmiento et al., 2004). Our data show that dCo is concurrently transported by this mechanism. However, at a depth of 2000 m dCo showed an abrupt change in concentration from elevated levels south of 43°S and much lower values to the north (Fig. 7b). The vertical profiles of dCo were similar among

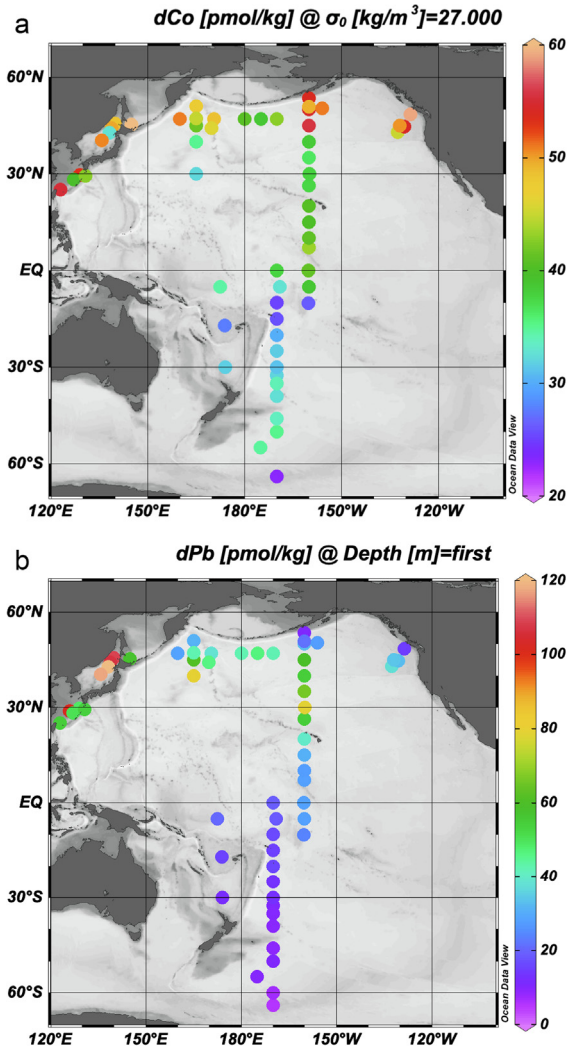

Fig. 8. Horizontal distribution of (a) dCo on an isopycnal plane of σ_0 = 27.0 and (b) dPb at the surface (~10 m depth). The data for the North Pacific, the East China Sea, and the Japan and Okhotsk Seas were acquired from (Zheng et al., 2019), (Nakaguchi et al., 2021), and (Nakaguchi et al., 2022), respectively.

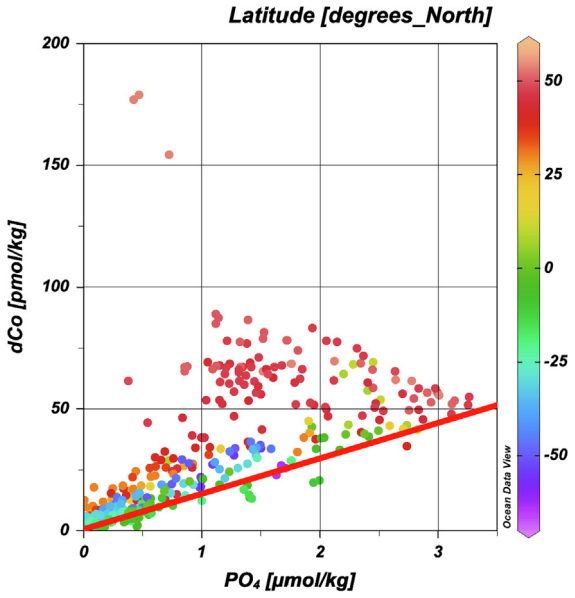

Fig. 9. Relationship between dCo and PO_4 in the upper water (σ_0 < 27.0) in the Pacific Ocean. The red line represents the regression line mentioned in the text. The dot color represents the latitude. (For interpretation of the references to color in this figure legend, the reader is referred to the web version of this article.)

the stations in the Fiji Basins and the Southwest Pacific Basin between 40°S and 15°S (Fig. 3e). The dCo concentrations at a depth of 2000 m were significantly lower at these stations than those at stations to the south of 43°S. Thus, it is likely that the transport of water and elements from the Fiji Basins to the Southwest Pacific Basin causes the abrupt change of dCo at 43°S.

The vertical distribution of the lpCo/tdCo ratio is shown in Supplementary Fig. 6c. Overall the lpCo/tdCo ratio was 0.28 ± 0.19 (n = 442) in the Pacific Ocean. However, because lpCo was ND in 60 % of samples in the South Pacific, the true value of the average should be lower. The lpCo/tdCo ratios generally increased with depth owing to scavenging, and significantly high ratios occurred around the Juan de Fuca Ridge (Zheng et al., 2017).

The distribution of dMn and dCo in surface water (Supplementary Fig. 9b, c) is important from the viewpoint of biological oceanography. To clarify the differences among the four trace metals, dM concentrations in surface water are plotted against latitude in Fig. 10. Because the surface mixed layer depth varied from 5 m to ~ 150 m at our stations, we show data from the surface to a depth of 60 m as a measure for basin-scale comparison. For comparison, the distribution of PO_4 is shown in Supplementary Fig. 10. The dMn concentration was highest at northernmost stations owing to supply from the continental shelf (Fig. 10c). The dMn concentration was higher than 0.2 nmol/kg at the stations to the north of 55°S, with concurrent maxima with dAl around 20°S and 20°N (Fig. 10a). This is probably because the supply rate of dMn by atmospheric deposition and currents overwhelms the removal rate of dMn by phytoplankton. The dCo concentration was highest at northernmost stations owing to supply from the continental shelf in a similar manner to dMn (Fig. 10d). However, dCo was depleted between 30°S and 30°N because of biological uptake. The dCo concentration increased southward to the south of 30°S owing to upwelling in the Southern Ocean. The ratios of dMn/PO_4 and dCo/PO_4 are plotted in Fig. 10e and 10f, respectively. The Mn/P and Co/P ratios in phytoplankton vary by 100 times or more between taxa and regions (Twining and Baines, 2013). As a measure, the average Mn/P and Co/P ratios for the cultured 15 marine eukaryotic phytoplankton species (Ho et al., 2003) are shown as dotted lines in Fig. 10e and 10f. The results suggest that dMn can be a co-limiting factor for the growth of phytoplankton around the equator and to the south of 40°S. These results are consistent with the Mn co-limitation of phytoplankton growth observed around the Drake Passage (Browning et al., 2021) and other regions. The results also show that dCo can be a co-limiting factor for phytoplankton growth in a wide area of the Pacific Ocean; whereby the cyanobacterium *Prochlorococcus* has developed minimal Co metabolism to thrive in Co-poor environments, such as the equatorial Pacific Ocean (Hawco et al., 2020). It is possible that our non-UV-dCo underestimates the bioavailable dCo. However, because UV-dCo is assumed to be less than the two times of non-UV-dCo (Supplementary Fig. 1), our conclusion of Co co-limiting will be valid for UV-dCo.

4.2.3. Lead

The sectional distribution of dPb from the South Pacific to the North Pacific is shown in Fig. 7c. The dPb maximum at each station occurred in a σ_0 range of 21.7–27.6 and a depth range of 10–596 m, which was shallower than that of dCo. A striking characteristic of the sectional distribution of dPb is a maximum in the Subtropical

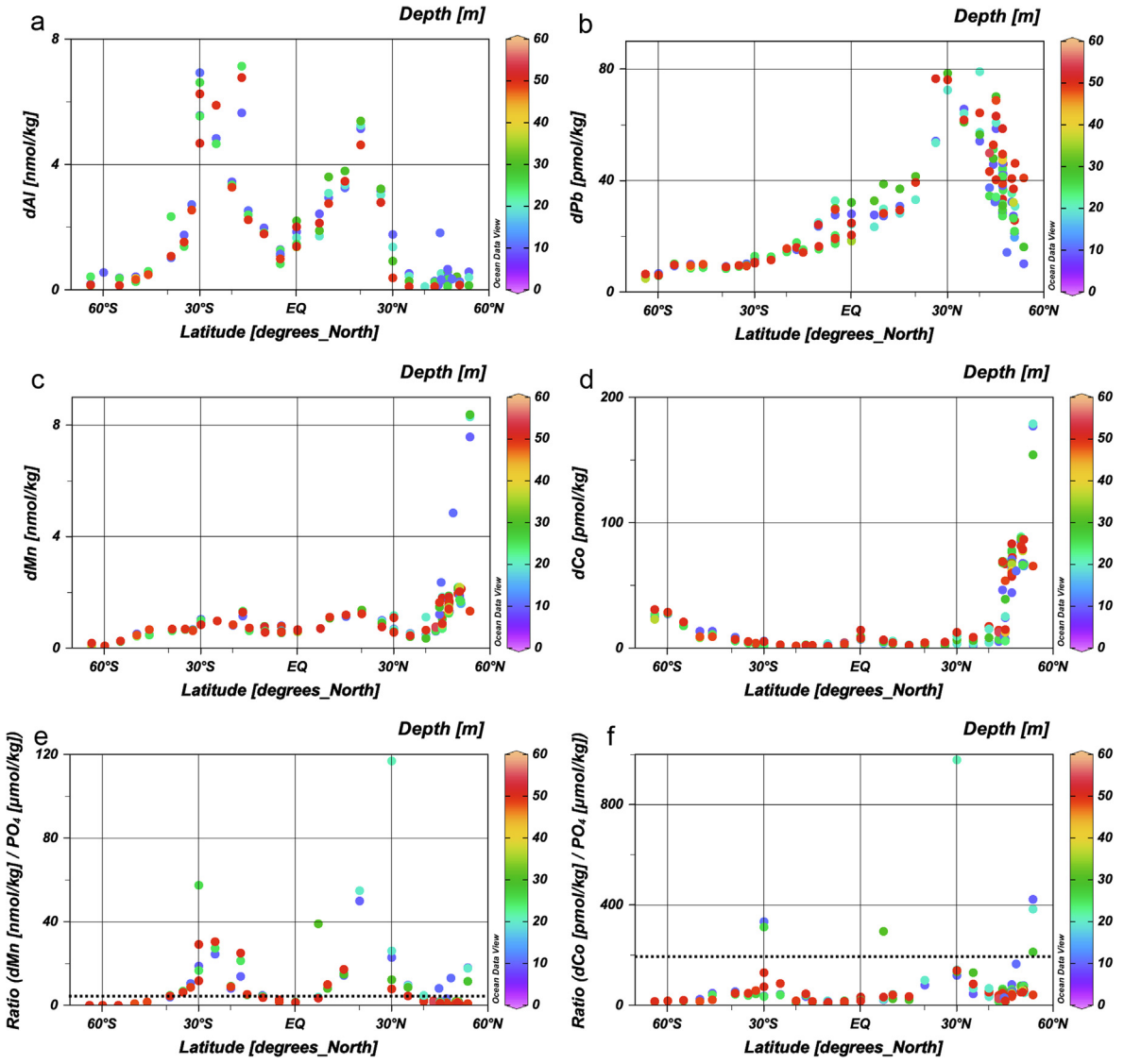

Fig. 10. Latitudinal distribution of parameters in the surface mixed layer (from surface to 60 m depth) in the Pacific Ocean. (a) dAl, (b) dPb, (c) dMn, (d) dCo, (e) dMn/PO_4 ratio ($\times 10^{-3}$), and (f) dCo/PO_4 ratio ($\times 10^{-6}$). The dot color represents the depth. The dotted lines in (e) and (f) represent the average Mn/P and Co/P ratios in cultured phytoplankton (Ho et al., 2003), respectively.

Mode Water (SMW) and Central Mode Water (CMW) with a depth of ~ 200 m between 25°–45°N. The horizontal distribution of dPb in surface water (~10 m depth) is shown in Fig. 8b, and the latitudinal distribution of dPb in the surface mixed layer is shown in Fig. 10b. These data are consistent with the fact that dPb is supplied from Asia and Russia as anthropogenic aerosols and transported by westerly winds to the North Pacific Ocean (Gallon et al., 2011; Zheng et al., 2019; Zurbrick et al., 2017). The dPb dissolved from aerosols is entrained in winter convection to form SMW and CMW, and then distributed throughout the North Pacific via subsurface water circulation. The dPb maximum is shallower than the dCo maximum because the vertical transport of dPb by biogenic particles is negligible.

There was a significant difference in dPb concentration between the North and South Pacific Oceans: 30 ± 20 pmol/kg (n = 566) in the North Pacific and 10 ± 6 pmol/kg (n = 397) in the South Pacific for all data of our study. The distribution of dPb indicates that Australia is a far smaller source than Asia and Russia. Aeolian transport of dPb from the Northern Hemisphere to the Southern Hemisphere is limited by the Hadley circulation.

In the South Pacific, dPb exhibited a linear relationship with dCo in deep water with $\sigma_\theta > 27.0$ (Supplementary Fig. 11):

$$\mathrm{dPb\,[pmol/kg]} = 0.446\,\mathrm{dCo\,[pmol/kg]} - 3.8 \quad (5)$$

$$R^2 = 0.889,\ n = 210$$

This linearity indicates that both dPb and dCo are concurrently scavenged from deep water and have no significant deep sources in this area. The slope was 42 % of that observed in the North Pacific. The high slope in the North Pacific is attributed to a high input flux of dPb.

The enrichment factor (EF) of dM in seawater over the upper crust is defined in accordance with the EF of M in aerosols in the literature (Rahn, 1976) as follows:

$$EF(\mathrm{dM}) = (\mathrm{dM/dAl})_{\mathrm{seawater}} / (\mathrm{M/Al})_{\mathrm{upper\ crust}} \quad (6)$$

The $(\mathrm{M/Al})_{\mathrm{upper\ crust}}$ is calculated in moles using concentrations published in a review (Rudnick and Gao, 2005) as follows: 2.7×10^{-5} for Pb, 4.7×10^{-3} for Mn, and 9.7×10^{-5} for Co. The vertical distribu-

tions of *EF*(dPb), *EF*(dMn), and *EF*(dCo) are shown in Supplementary Fig. 12. In general, *EF*(dPb), *EF*(dMn), and *EF*(dCo) decreased with depth. *EF*(dM) showed relatively small variations below 4500 m owing to the northward flow of the LCDW: *EF*(dPb) = 94 ± 85 (n = 63), *EF*(dMn) = 26 ± 31 (n = 66), and *EF*(dCo) = 70 ± 41 (n = 65). In the upper water, *EF*(dM) was substantially higher in the North Pacific. This is because these three elements have a major source in the North Pacific. Particularly, the difference between the North and South Pacific was largest in *EF*(dPb): 40–24000 (3400 ± 4400, n = 401) in the North Pacific and 13–2600 (270 ± 350, n = 326) in the South Pacific above the 4500 m depth. The average in the North Pacific was three times higher than the average of aerosol *EF* recently observed in the North Atlantic (Shelley et al., 2015). The difference in *EF*(dPb) between the North and South Pacific is partly because the history of significant environmental Pb pollution has extended over the past 200 years (Boyle et al., 2014). It is possible that the global overturning circulation through the Pacific and Southern Oceans (Talley, 2013) will reduce the difference in *EF*(dPb) between the North and South Pacific in the future. In addition, it is possible that anthropogenic pollution also contributes to high *EF*(dMn) and *EF*(dCo) values in the North Pacific. However, we cannot deny other mechanisms. Another possible mechanism is that dust inputs have been enhanced in the North Pacific due to climate change and the dust inputs and photoreduction processes may result in enhanced dMn and dCo concentrations over crustal values.

5. Conclusions

In this study, the data of multi-elements with speciation of dissolved and particulate species enable further understanding of the biogeochemical cycling of scavenged elements. Dissolved Al, dMn, dCo, and dPb are distributed differently in the Pacific Ocean due to different major sources and different biogeochemical cycling. The major source of dAl is Australia and islands in the South Pacific. Based on our data, we propose a hypothesis, that is, kaolinite-dominated sediments yield near-bottom maxima of dAl in the Fiji Basins and the Southwest Pacific Basin. This mechanism makes the western South Pacific a substantial source of dAl over the entire Pacific Ocean. Our hypothesis suggests a tight connection between the weathering on land and the distribution of dAl in the Pacific Ocean. In contrast, strong sources of dMn, dCo, and dPb occur in the North Pacific. The major source of dMn and dCo is continental shelf sediments, and the major source of dPb is anthropogenic aerosols. Dissolved Co shows a necklace-like maximum in intermediate waters on the meridional sectional distribution, which is sustained by biogeochemical transport in the upper water and scavenging in the deep water. The dMn/PO_4 and dCo/PO_4 ratios in the surface mixed layer indicate that dCo is deficient for phytoplankton in a large area of the Pacific, although dMn is deficient only around the equator and to the south of the STF. Dissolved Pb is highly concentrated in the North Pacific with high *EF*(dPb) values, indicating that anthropogenic pollution dominates the oceanic distribution of dPb. In addition, *EF*(dMn) and *EF*(dCo) have significantly high values in the upper waters of the North Pacific, implying the possible effects of anthropogenic pollution on the distribution of dMn and dCo. Also, particulate species show significant difference among the four metals. The fraction of lpM decreases in the order of Al > Mn > Co > Pb. The distributions of lpAl, lpMn, and lpCo show a similarity, suggesting the dominant effect of lithogenic particles. However, the lpMn/lpAl ratio is ten times higher than the upper crustal Mn/Al ratio due to extensive scavenging of dMn. Labile particulate Co shows surface maxima due to uptake by phytoplankton.

The scavenged elements are useful tracers of the modern ocean circulation. It is possible that they will be useful tracers of the ocean change. When global warming intensifies weathering and increases the supply of kaolinite to the western South Pacific, the near-bottom maximum of dAl will be enhanced in the Pacific Ocean. The effect of anthropogenic pollution on the distribution of dPb is apparent in the North Pacific today. This effect may progressively propagate into the South Pacific via ocean circulation in the future.

Data availability

The data are given in the supplementary files.

Declaration of Competing Interest

The authors declare that they have no known competing financial interests or personal relationships that could have appeared to influence the work reported in this paper.

Acknowledgments

The authors thank the crew, technicians, students, and scientists onboard the KH-14-6 cruise for assistance with the sampling and analysis of routine data. This research was supported by the Japan Society for the Promotion of Science (JSPS) KAKENHI grants (24241004, 15H01727, and 19H01148 to YS; 21 K17877 to LZ) and by Mitsumasa Ito Memorial Research Grants from the Research Institute for Oceanochemistry Foundation (H29-R1 to TM; H31-R1 and R2-R2 to LZ). We would like to thank Editage (www.editage.jp) for the English language editing.

Appendix A. Supplementary material

Supplementary material to this article can be found online at https://doi.org/10.1016/j.gca.2022.10.022.

Data availability The data are given in the supplementary files

References

Baumberger, T., Lilley, M.D., Lupton, J.E., Baker, E.T., Resing, J.A., Buck, N.J., Walker, S. L., Früh-Green, G.L., 2020. Dissolved Gas and Metal Composition of Hydrothermal Plumes From a 2008 Submarine Eruption on the Northeast Lau Spreading Center. Front. Mar. Sci. 7, 171.

Biller, D.V., Bruland, K.W., 2012. Analysis of Mn, Fe Co, Ni, Cu, Zn, Cd, and Pb in seawater using the Nobias-chelate PA1 resin and magnetic sector inductively coupled plasma mass spectrometry (ICP-MS). Mar. Chem. 130–131, 12–20.

Bostock, H.C., Opdyke, B.N., Williams, M.J.M., 2010. Characterising the intermediate depth waters of the Pacific Ocean using $\delta^{13}C$ and other geochemical tracers. Deep-Sea Res. I 57, 847–859.

Bown, J., Boye, M., Baker, A., Duvieilbourg, E., Lacan, F., Le Moigne, F., Planchon, F., Speich, S., Nelson, D.M., 2011. The biogeochemical cycle of dissolved cobalt in the Atlantic and the Southern Ocean south off the coast of South Africa. Mar. Chem. 126, 193–206.

Boyle, E., Lee, J.-M., Echegoyen, Y., Noble, A., Moos, S., Carrasco, G., Zhao, N., Kayser, R., Zhang, J., Gamo, T., Obata, H., Norisuye, K., 2014. Anthropogenic lead emissions in the ocean: The evolving global experiment. Oceanography 27, 69–75.

Boyle, E.A., Zurbrick, C., Lee, J.-M., Till, R., Till, C.P., Zhang, J., Flegal, A.R., 2020. Lead and lead isotopes in the U.S. GEOTRACES East Pacific zonal transect (GEOTRACES GP16). Mar. Chem. 227, 103892.

Brimhall, G.H., Christopher, J.L., Ford, C., Bratt, J., Taylor, G., Warin, O., 1991. Quantitative geochemical approach to pedogenesis: importance of parent material reduction, volumetric expansion, and eolian influx in lateritization. Geoderma 51, 51–91.

Browning, T.J., Achterberg, E.P., Engel, A., Mawji, E., 2021. Manganese co-limitation of phytoplankton growth and major nutrient drawdown in the Southern Ocean. Nat. Commun. 12, 884.

Bruland, K.W., Lohan, M.C., 2003. Controls of trace metals in seawater. In: Elderfield, H. (Ed.), The Oceans and Marine Geochemistry. Elsevier-Pergamon, Oxford, pp. 23–47.

Buck, C.S., Landing, W.M., Resing, J., 2013. Pacific Ocean aerosols: Deposition and solubility of iron, aluminum, and other trace elements. Mar. Chem. 157, 117–130.
Butler, E.C.V., O'Sullivan, J.E., Watson, R.J., Bowie, A.R., Remenyi, T.A., Lannuzel, D., 2013. Trace metals Cd Co, Cu, Ni, and Zn in waters of the subantarctic and Polar Frontal Zones south of Tasmania during the 'SAZ-Sense' project. Mar. Chem. 148, 63–76.
Chen, G., Wu, J., 2019. Meridional distribution of dissolved manganese in the tropical and equatorial pacific. Geochim. Cosmochim. Acta 263, 50–67.
Chester, R., 2000. Marine Geochemistry. Blackwell, Malden.
Chmiel, R., Lanning, N., Laubach, A., Lee, J.M., Fitzsimmons, J., Hatta, M., Jenkins, W.J., Lam, P.J., McIlvin, M., Tagliabue, A., Saito, M.A., 2021. Major processes of the dissolved cobalt cycle in the North and equatorial Pacific Ocean. Biogeosciences Discuss. 2021, 1–45.
Cid, A.P., Urushihara, S., Minami, T., Norisuye, K., Sohrin, Y., 2011. Stoichiometry among bioactive trace metals in seawater on the Bering Sea shelf. J. Oceanogr. 67, 747–764.
Cid, A.P., Nakatsuka, S., Sohrin, Y., 2012. Stoichiometry among bioactive trace metals in the Chukchi and Beaufort Seas. J. Oceanogr. 68, 985–1001.
Cohen, N.R., Noble, A.E., Moran, D.M., McIlvin, M.R., Goepfert, T.J., Hawco, N.J., German, C.R., Horner, T.J., Lamborg, C.H., McCrow, J.P., Allen, A.E., Saito, M.A., 2021. Hydrothermal trace metal release and microbial metabolism in the northeastern Lau Basin of the South Pacific Ocean. Biogeosciences 18, 5397–5422.
Ellwood, M.J., 2008. Wintertime trace metal (Zn, Cu, Ni, Cd, Pb and Co) and nutrient distributions in the Subantarctic Zone between 40–52°S; 155–160°E. Mar. Chem. 112, 107–117.
Gallon, C., Ranville, M.A., Conaway, C.H., Landing, W.M., Buck, C.S., Morton, P.L., Flegal, A.R., 2011. Asian industrial lead inputs to the north pacific evidenced by lead concentrations and isotopic compositions in surface waters and aerosols. Environ. Sci. Technol. 45, 9874–9882.
Gehlen, M., Beck, L., Calas, G., Flank, A.M., Van Bennekom, A.J., Van Beusekom, J.E.E., 2002. Unraveling the atomic structure of biogenic silica: evidence of the structural association of Al and Si in diatom frustules. Geochim. Cosmochim. Acta 66, 1601–1609.
Griffin, J.J., Windom, H., Goldberg, E.D., 1968. The distribution of clay minerals in the World Ocean. Deep-Sea Res. 15, 433–459.
Hawco, N.J., Ohnemus, D.C., Resing, J.A., Twining, B.S., Saito, M.A., 2016. A dissolved cobalt plume in the oxygen minimum zone of the eastern tropical South Pacific. Biogeosciences 13, 5697–5717.
Hawco, N.J., Lam, P.J., Lee, J.-M., Ohnemus, D.C., Noble, A.E., Wyatt, N.J., Lohan, M.C., Saito, M.A., 2018. Cobalt scavenging in the mesopelagic ocean and its influence on global mass balance: Synthesizing water column and sedimentary fluxes. Mar. Chem. 201, 151–166.
Hawco, N.J., McIlvin, M.M., Bundy, R.M., Tagliabue, A., Goepfert, T.J., Moran, D.M., Valentin-Alvarado, L., DiTullio, G.R., Saito, M.A., 2020. Minimal cobalt metabolism in the marine cyanobacterium *Prochlorococcus*. Proc. Natl. Acad. Sci.
Ho, T.-Y., Quigg, A., Finkel, Z.V., Milligan, A.J., Wyman, K., Falkowski, P.G., Morel, F.M. M., 2003. The elemental composition of some marine phytoplankton. J. Phycol. 39, 1145–1159.
Ho, P., Resing, J.A., Shiller, A.M., 2019. Processes controlling the distribution of dissolved Al and Ga along the U.S. GEOTRACES East Pacific Zonal Transect (GP16). Deep-Sea Res. I 147, 128–145.
Jenkins, W.J., Doney, S.C., Fendrock, M., Fine, R., Gamo, T., Jean-Baptiste, P., Key, R., Klein, B., Lupton, J.E., Newton, R., Rhein, M., Roether, W., Sano, Y., Schlitzer, R., Schlosser, P., Swift, J., 2019. A comprehensive global oceanic dataset of helium isotope and tritium measurements. Earth Syst. Sci. Data 11, 441–454.
Jenkins, W.J., Hatta, M., Fitzsimmons, J.N., Schlitzer, R., Lanning, N.T., Shiller, A., Buckley, N.R., German, C.R., Lott, D.E., Weiss, G., Whitmore, L., Casciotti, K., Lam, P.J., Cutter, G.A., Cahill, K.L., 2020. An intermediate-depth source of hydrothermal ^{3}He and dissolved iron in the North Pacific. Earth Planet. Sci. Lett. 539, 116223.
Kaupp, L.J., Measures, C.I., Selph, K.E., Mackenzie, F.T., 2011. The distribution of dissolved Fe and Al in the upper waters of the Eastern Equatorial Pacific. Deep-Sea Res. II 58, 296–310.
Kawabe, M., Fujio, S., 2010. Pacific Ocean circulation based on observation. J. Oceanogr. 66, 389–403.
Khawmee, K., Suddhiprakarn, A., Kheoruenromne, I., Bibi, I., Singh, B., 2013. Dissolution behaviour of soil kaolinites in acidic solutions. Clay Miner. 48, 447–461.
Knap, A.H., Michaels, A., Close, A.R., Ducklow, H., Dickson, A.G., 1996. Protocols for the Joint Global Ocean Flux Study (JGOFS) Core Measurements.
Koning, E., Epping, E., Van Raaphorst, W., 2002. Determining biogenic silica in marine samples by tracking silicate and aluminium concentrations in alkaline leaching solutions. Aquat. Geochem. 8, 37–67.
Lam, P.J., Lee, J.-M., Heller, M.I., Mehic, S., Xiang, Y., Bates, N.R., 2018. Size-fractionated distributions of suspended particle concentration and major phase composition from the U.S. GEOTRACES Eastern Pacific Zonal Transect (GP16). Mar. Chem. 201, 90–107.
Lupton, J.E., Pyle, D.G., Jenkins, W.J., Greene, R., Evans, L., 2004. Evidence for an extensive hydrothermal plume in the Tonga-Fiji region of the South Pacific. Geochem. Geophys. Geosyst. 5, Q01003.
Lupton, J., Rubin, K.H., Arculus, R., Lilley, M., Butterfield, D., Resing, J., Baker, E., Embley, R., 2015. Helium isotope, C/^{3}He, and Ba-Nb-Ti signatures in the northern Lau Basin: Distinguishing arc, back-arc, and hotspot affinities. Geochem. Geophys. Geosyst. 16, 1133–1155.
Measures, C.I., Hatta, M., 2021. On using Si to unravel potential sources of dissolved Al to the deep Arctic. J. Geophys. Res. Oceans 126. e2021JC017399.
Measures, C., Hatta, M., Fitzsimmons, J., Morton, P., 2015. Dissolved Al in the zonal N Atlantic section of the US GEOTRACES 2010/2011 cruises and the importance of hydrothermal inputs. Deep-Sea Res. II 116, 176–186.
Measures, C.I., Vink, S., 2000. On the use of dissolved aluminum in surface waters to estimate dust deposition to the ocean. Global Biogeochem. Cycles 14, 317–327.
Menzel Barraqueta, J.L., Klar, J.K., Gledhill, M., Schlosser, C., Shelley, R., Planquette, H.F., Wenzel, B., Sarthou, G., Achterberg, E.P., 2019. Atmospheric deposition fluxes over the Atlantic Ocean: a GEOTRACES case study. Biogeosciences 16, 1525–1542.
Menzel Barraqueta, J.-L., Samanta, S., Achterberg, E.P., Bowie, A.R., Croot, P., Cloete, R., De Jongh, T., Gelado-Caballero, M.D., Klar, J.K., Middag, R., Loock, J.C., Remenyi, T.A., Wenzel, B., Roychoudhury, A.N., 2020. A first global oceanic compilation of observational dissolved aluminum data with regional statistical data treatment. Front. Mar. Sci. 7, 468.
Middag, R., de Baar, H.J.W., Laan, P., Bakker, K., 2009. Dissolved aluminium and the silicon cycle in the Arctic Ocean. Mar. Chem. 115, 176–195.
Middag, R., van Slooten, C., de Baar, H.J.W., Laan, P., 2011. Dissolved aluminium in the Southern Ocean. Deep-Sea Res. II 58, 2647–2660.
Middag, R., de Baar, H.J.W., Laan, P., Huhn, O., 2012. The effects of continental margins and water mass circulation on the distribution of dissolved aluminum and manganese in Drake Passage. J. Geophys. Res. 117, C01019.
Middag, R., van Hulten, M.M.P., Van Aken, H.M., Rijkenberg, M.J.A., Gerringa, L.J.A., Laan, P., de Baar, H.J.W., 2015. Dissolved aluminium in the ocean conveyor of the West Atlantic Ocean: Effects of the biological cycle, scavenging, sediment resuspension and hydrography. Mar. Chem. 177, 69–86.
Milliman, J.D., Farnsworth, K.L., Albertin, C.S., 1999. Flux and fate of fluvial sediments leaving large islands in the East Indies. J. Sea Res. 41, 97–107.
Milne, A., Landing, W., Bizimis, M., Morton, P., 2010. Determination of Mn, Fe Co, Ni, Cu, Zn, Cd and Pb in seawater using high resolution magnetic sector inductively coupled mass spectrometry (HR-ICP-MS). Anal. Chim. Acta 665, 200–207.
Minami, T., Konagaya, W., Zheng, L., Takano, S., Sasaki, M., Murata, R., Nakaguchi, Y., Sohrin, Y., 2015. An off-line automated preconcentration system with ethylenediaminetriacetate chelating resin for the determination of trace metals in seawater by high-resolution inductively coupled plasma mass spectrometry. Anal. Chim. Acta 854, 183–190.
Moffett, J.W., Ho, J., 1996. Oxidation of cobalt and manganese in seawater via a common microbially catalyzed pathway. Geochim. Cosmochim. Acta 60, 3415–3424.
Nakaguchi, Y., Ikeda, Y., Sakamoto, A., Zheng, L., Minami, T., Sohrin, Y., 2021. Distribution and stoichiometry of Al, Mn, Fe Co, Ni, Cu, Zn, Cd, and Pb in the East China Sea. J. Oceanogr. 77, 463–485.
Nakaguchi, Y., Sakamoto, A., Asatani, T., Minami, T., Shitashima, K., Zheng, L., Sohrin, Y., 2022. Distribution and stoichiometry of Al, Mn, Fe Co, Ni, Cu, Zn, Cd, and Pb in the Seas of Japan and Okhotsk. Mar. Chem. 241, 104108.
Pichler, T., Ridley, W.I., Nelson, E., 1999. Low-temperature alteration of dredged volcanics from the Southern Chile Ridge: additional information about early stages of seafloor weathering. Mar. Geol. 159, 155–177.
Pinedo-González, P., West, A.J., Tovar-Sanchez, A., Duarte, C.M., Sañudo-Wilhelmy, S.A., 2018. Concentration and isotopic composition of dissolved Pb in surface waters of the modern global ocean. Geochim. Cosmochim. Acta 235, 41–54.
Rahn, K.A., 1976. Silicon and aluminum in atmospheric aerosols: Crust-air fractionation? Atmos. Environ. 10, 597–601.
Reid, J.L., 1986. On the total geostrophic circulation of the South Pacific Ocean: Flow patterns, tracers and transports. Progr. Oceanogr. 16, 1–61.
Reid, J.L., 1997. On the total geostrophic circulation of the pacific ocean: flow patterns, tracers, and transports. Progr. Oceanogr. 39, 263–352.
Remenyi, T., Nesterenko, P., Bowie, A., Butler, E., Haddad, P., 2012. Reversed phase high performance liquid chromatographic determination of dissolved aluminium in open ocean seawater. Limnol. Oceanogr. Methods 10, 832–839.
Resing, J.A., Sedwick, P.N., German, C.R., Jenkins, W.J., Moffett, J.W., Sohst, B.M., Tagliabue, A., 2015. Basin-scale transport of hydrothermal dissolved metals across the South Pacific Ocean. Nature 523, 200–203.
Rudnick, R.L., Gao, S., 2005. Composition of the continental crust. In: Rudnick, R.L. (Ed.), The Crust. Elsevier-Pergamon, Oxford, pp. 1–64.
Saito, M.A., Moffett, J.W., 2001. Complexation of cobalt by natural organic ligands in the Sargasso Sea as determined by a new high-sensitivity electrochemical cobalt speciation method suitable for open ocean work. Mar. Chem. 75, 49–68.
Sarmiento, J.L., Gruber, N., Brzezinski, M.A., Dunne, J.P., 2004. High-latitude controls of thermocline nutrients and low latitude biological productivity. Nature 427, 56–60.
Schlitzer, R., 2007. Assimilation of radiocarbon and chlorofluorocarbon data to constrain deep and bottom water transports in the world ocean. J. Phys. Oceanogr. 37, 259–276.
Schlitzer, R., 2021. Ocean Data View. https://odv.awi.de.
Sedwick, P.N., Gamo, T., McMurtry, G.M., 1990. Manganese and methane anomalies in the North Fiji Basin. Deep-Sea Res. A 37, 891–896.
Shelley, R.U., Morton, P.L., Landing, W.M., 2015. Elemental ratios and enrichment factors in aerosols from the US-GEOTRACES North Atlantic transects. Deep-Sea Res. II 116, 262–272.
Sholkovitz, E.R., Elderfield, H., Szymczak, R., Casey, K., 1999. Island weathering: river sources of rare earth elements to the Western Pacific Ocean. Mar. Chem. 68, 39–57.
Sieber, M., Conway, T.M., de Souza, G.F., Obata, H., Takano, S., Sohrin, Y., Vance, D., 2019. Physical and biogeochemical controls on the distribution of dissolved

cadmium and its isotopes in the Southwest Pacific Ocean. Chem. Geol. 511, 494–509.
Slemons, L., Paul, B., Resing, J., Murray, J.W., 2012. Particulate iron, aluminum, and manganese in the Pacific equatorial undercurrent and low latitude western boundary current sources. Mar. Chem. 142–144, 54–67.
Sohrin, Y., Bruland, K.W., 2011. Global status of trace elements in the ocean. Trends Anal. Chem. 30, 1291–1307.
Sunda, W.G., Huntsman, S.A., 1994. Photoreduction of manganese oxides in seawater. Mar. Chem. 46, 133–152.
Talley, L.D., 2013. Closure of the global overturning circulation through the Indian, Pacific, and Southern Oceans: Schematics and transports. Oceanography 26, 80–97.
Talley, L.D., Pickard, G.L., Emery, W.J., Swift, J.H., 2011. Descriptive Physical Oceanography: An Introduction. Elsevier, Amsterdam.
Twining, B.S., Baines, S.B., 2013. The trace metal composition of marine phytoplankton. Annu. Rev. Mar. Sci. 5, 191–215.
van Hulten, M., Middag, R., Dutay, J.C., de Baar, H., Roy-Barman, M., Gehlen, M., Tagliabue, A., Sterl, A., 2017. Manganese in the west Atlantic Ocean in the context of the first global ocean circulation model of manganese. Biogeosciences 14, 1123–1152.
van Hulten, M.M.P., Sterl, A., Middag, R., de Baar, H.J.W., Gehlen, M., Dutay, J.C., Tagliabue, A., 2014. On the effects of circulation, sediment resuspension and biological incorporation by diatoms in an ocean model of aluminium. Biogeosciences 11, 3757–3779.
von Langen, P.J., Johnson, K.S., Coale, K.H., Elrod, V.A., 1997. Oxidation kinetics of manganese (II) in seawater at nanomolar concentrations. Geochim. Cosmochim. Acta 61, 4945–4954.
Vu, H.T.D., Sohrin, Y., 2013. Diverse stoichiometry of dissolved trace metals in the Indian Ocean. Sci. Rep. 3, 1745.
Wu, J., Rember, R., Jin, M., Boyle, E.A., Flegal, A.R., 2010. Isotopic evidence for the source of lead in the North Pacific abyssal water. Geochim. Cosmochim. Acta 74, 4629–4638.
Wuttig, K., Townsend, A.T., van der Merwe, P., Gault-Ringold, M., Holmes, T., Schallenberg, C., Latour, P., Tonnard, M., Rijkenberg, M.J.A., Lannuzel, D., Bowie, A.R., 2019. Critical evaluation of a sea*FAST* system for the analysis of trace metals in marine samples. Talanta 197, 653–668.
Yang, L., Nadeau, K., Meija, J., Grinberg, P., Pagliano, E., Ardini, F., Grotti, M., Schlosser, C., Streu, P., Achterberg, E.P., Sohrin, Y., Minami, T., Zheng, L., Wu, J., Chen, G., Ellwood, M.J., Turetta, C., Aguilar-Islas, A., Rember, R., Sarthou, G., Tonnard, M., Planquette, H., Matoušek, T., Crum, S., Mester, Z., 2018. Inter-laboratory study for the certification of trace elements in seawater certified reference materials NASS-7 and CASS-6. Anal. Bioanal. Chem. 410, 4469–4479.
Yuen, D.A., Scruggs, M.A., Spera, F.J., Zheng, Y., Hu, H., McNutt, S.R., Thompson, G., Mandli, K., Keller, B.R., Wei, S.S., Peng, Z., Zhou, Z., Mulargia, F., Tanioka, Y., 2022. Under the surface: Pressure-induced planetary-scale waves, volcanic lightning, and gaseous clouds caused by the submarine eruption of Hunga Tonga-Hunga Ha'apai volcano. Earthq. Res. Adv. 2, 100134.
Zhang, Y., Mahowald, N., Scanza, R.A., Journet, E., Desboeufs, K., Albani, S., Kok, J.F., Zhuang, G., Chen, Y., Cohen, D.D., Paytan, A., Patey, M.D., Achterberg, E.P., Engelbrecht, J.P., Fomba, K.W., 2015. Modeling the global emission, transport and deposition of trace elements associated with mineral dust. Biogeosciences 12, 5771–5792.
Zheng, L., Minami, T., Takano, S., Minami, H., Sohrin, Y., 2017. Distribution and stoichiometry of Al, Mn, Fe Co, Ni, Cu, Zn, Cd, and Pb in seawater around the Juan de Fuca Ridge. J. Oceanogr. 73, 669–685.
Zheng, L., Minami, T., Konagaya, W., Chan, C.-Y., Tsujisaka, M., Takano, S., Norisuye, K., Sohrin, Y., 2019. Distinct basin-scale-distributions of aluminum, manganese, cobalt, and lead in the North Pacific Ocean. Geochim. Cosmochim. Acta 254, 102–121.
Zurbrick, C.M., Gallon, C., Flegal, A.R., 2017. Historic and industrial lead within the Northwest Pacific Ocean evidenced by lead isotopes in seawater. Environ. Sci. Technol. 51, 1203–1212.